MODELING OF MAGNETIC NANOPARTICLES TRANSPORT IN SHALE RESERVOIRS

A Thesis

by

CHENG AN

Submitted to the Office of Graduate and Professional Studies of
Texas A&M University
in partial fulfillment of the requirements for the degree of

MASTER OF SCIENCE

Chair of Committee,	John E. Killough
Committee Members,	Walter Ayers
	Yuefeng Sun
Head of Department,	A. Daniel Hill

December 2014

Major Subject: Petroleum Engineering

ABSTRACT

Currently, the application of nanoparticles has attracted much attention due to the potential of nanotechnology to lead to evolutionary changes in the petroleum industry. The literature contains numerous references to the possible use of this technology for enhanced oil recovery, nano-scale sensors and subsurface mapping. Little work has been conducted to establish numerical models to investigate nanoparticle transport in reservoirs, and particularly much less for shale reservoirs. Unlike conventional reservoirs, shale formations are usually made up of four pores systems: inorganic matter, organic matter dominated by hydrocarbon wettability, natural fractures and hydraulic fractures. Concurrently, hydraulic fractures and the associated stimulated reservoir volume (SRV) from induced fractures play a critical role in significantly increasing well productivity.

In this project, a mathematical model for simulating nanoparticle transport in shale reservoirs was developed. The simulator includes contributions from Darcy flow, Brownian diffusion, gas diffusion and desorption, slippage flow, and capillary effects based on the extremely low permeability and micro- to nano-scale of the pores. Moreover, these diverse mechanisms are separately applied to different portions of the reservoir due to the variation in media properties. Applications of the model include numerical examples from two-dimensional micro models to macro models, both with organic matter randomly distributed within the inorganic matrix. The effects of varying water saturation, grid pressure, and mass concentration of nanoparticles are

shown graphically in these numerical examples. The main conclusion from these models is that, as expected, nanoparticles can only easily flow along with the aqueous phase into the fractures, but their transport into the shale matrix is quite limited, with little transport shown into the organic matter. In addition, based on the magnetic properties of synthesized magnetic carbon-coated iron-oxide nanoparticles, the distribution of the volumetric magnetic susceptibility and the magnetization of reservoir including SRV are simulated and displayed in the numerical cases with and without magnetic nanoparticles. The numerical results demonstrate that magnetic nanoparticles can effectively increase the magnetic susceptibility and the magnetization of reservoir thus producing enhanced signals from well logging devices such as NMR and leading to improved reservoir and fracture characterization. This simulator can provide the benefits of both numerically simulating the transport and distribution of nanoparticles in hydraulically fractured shale formations and supplying helpful guidelines of nanoparticles injection plans to enhance well logging signals. Furthermore, this model can also allow us to mimic the tracer transport flow in unconventional reservoirs.

DEDICATION

To my beloved parents and my darling girlfriend

To people who have even helped and supported me

ACKNOWLEDGEMENTS

I would like to give my sincere gratitude to my supervisor, Dr. John Killough, for his excellent technique guidance, care, patience and everything else. I also want to thank my committee members, Dr. Walter Ayers and Dr. Yuefeng Sun, and co-chair of this nanoparticle project, Dr. Zoya Heidari for their support and assistance throughout this research.

I would also like to thank The Crisman Institute at Petroleum Engineering Department of Texas A&M University for funding this project. Many thanks also go to my friends and officemates for providing a comfortable and awesome research atmosphere, especially for Bicheng Yan and Masoud Alfi, Abdulhamed Alfaleh, Yang Cao, Jie He, Sunhua Gao, Zhi Chai, and Hongqing Song. It was really great experience to study together and discuss research with them.

Finally, I like take this chance to show my deepest gratitude to my father and mother and my girlfriend for their unconditional care, support and understanding all the time.

NOMENCLATURE

A_{nm}	Interface between Grid m and n
C_{vol}	Volume Magnetic Susceptibility
D_e	Diffusion Coefficient of Nanoparticles
F_{nm}	Average Value of Normal Flux from Grid m and n
K_b	Boltzmann Constant
M_t	Total Mass of Nanoparticles
M_{total}	Total Magnetization of Reservoir
N_{inorg}	Number of Inorganic Matter in the Mesh
N_{krg}	Number of Kerogen Grids in the Mesh
P_c	Capillary Pressure
P_e	Capillary Entry Pressure
Q_{Nano}	Source and Sink of Nanoparticles
S_e	Effective Water Saturation
S_{wr}	Residual Wetting Phase Saturation
S_β	Saturation of Phase β
V_m	Volume of Grid m
V_n	Volume of Grid n
Vol_i	Volume of Grid i
X_β^l	Mass Fraction of Component l in the Phase β

d_m	Distance from the Center Point of Grid m to the Interface
d_n	Distance from the Center Point of Grid n to the Interface
d_p	Diameter of Nanoparticles
g_{nm}	Gravitational Acceleration in the Direction from m to n
$k_{r\beta}$	Relative Permeability to the Phase β
m_{NPs}	Mass of Nanoparticles
x_m	Volume Magnetic Susceptibility
μ_{eff}	Effective Magnetic Moment per Paramagnetic Ion
μ_β	Viscosity of Phase β
ρ_{inorg}	Density of Inorganic Matter
ρ_{krg}	Density of Kerogen Matter
ρ_β	Density of Phase β
ϕ_{inorg}	Porosity of Inorganic Matter
ϕ_{krg}	Porosity of Kerogen Matter
Δt	Time Step Size
D	Dimension
EIA	Energy Information Administration
NMR	Nuclear Magnetic Resonance
SEM	Scanning Electron Microscope
SRV	Stimulated Reservoir Volume
TOC	Total Organic Carbon

C	Concentration of Nanoparticles
F	Flux of Component
H	Iteration Index
H	Magnetic Field Strength
M	Mass of Accumulation of Component
MSL	Magnetic Susceptibility Loop
NPs	Nanoparticles
Q	Source and Sink of Component
R	Residual
T	Absolute Temperature
b	Klinkenberg Factor
k	Absolute Permeability of Porous Media
l	Index of Component
mD	Millidarcy
nD	Nanodarcy
t	Time
β	Index of Phase
ϕ	Porosity of Porous Media

TABLE OF CONTENTS

Page

LIST OF FIGURES

Page

LIST OF TABLES

Page

CHAPTER I

INTRODUCTION AND LITERATURE REVIEW

1.1 Problem Statement

Due to the advance revolution and potential advantages of nanotechnology, magnetic nanoparticles have been investigated to enhance signals from well logging such as NMR and improve reservoir and fracture characterization. The study of nanoparticle transport in porous media is a critical issue for both reservoir applications and environmental concerns. Little work has been performed with nanoparticles transport in unconventional reservoirs, such as shales. Taking into account of various components of shale reservoirs and complex flow mechanisms in different pores systems, a solid mathematic model looking at two-phase flow carrying nanoparticles is required for better understanding the transport process of nanoparticles in shale reservoirs. In addition, this simulator should be also capable of achieving these functions as following:

(1) Due to the existence of kerogen matter and micro-scale and nano-scale pores in shale reservoirs, the simulator should incorporate and consider various flow mechanisms such as Darcy flow, Brownian diffusion, gas diffusion and desorption, slippage flow, and capillary pressure effects for different pore systems.

(2) Except for the changing trend of pressure, water saturation, and nanoparticles concentration, this simulator should also be capable of showing the distribution of

volumetric magnetic susceptibility and magnetization of the reservoir and then validate the goal of enhancing logging signals by comparing with the experimental results.

(3) This simulator is also supposed to perform sensitivity analysis, find the influence of various parameters such as organic matter, Brownian diffusion, the size and magnetism of nanoparticles and fractures patterns, and obtain the optimal condition for our purposes at diverse reservoir situation.

1.2 Background and Literature Review

The total volume of fossil fuel reserves worldwide was believed to be on the decline due to the reduced incidence of significant discoveries of oil & gas reservoirs worldwide. In addition, the continuously decrease of easily recoverable oil and gas reserves and the complicated political relationship in those critical oil supplying countries, to economically and effectively explore unconventional reservoirs become more and more important and urgent. The Annual Energy Outlook 2013 (AEO) from the U.S. Dept. of Energy's Energy Information Administrations has already highlighted the importance of unconventional shale gas and shale oil production in the U.S. domestic oil and gas production. Unconventional reservoirs are hydrocarbon reservoirs that have low permeability and porosity, such as shale gas reservoirs, bed methane reservoirs, and tight gas reservoirs. Based on the significant technical breakthroughs including horizontal drilling and hydraulic fracturing, matrix permeability of reservoirs becomes available and commercial from millidarcies in conventional reservoirs to microdarcies in tight gas

reservoirs down to nanodarcies in shale gas reservoirs (Kundert et al. 2009 and Arogundade et al. 2012). As suggested by Energy Information Administration (Figure 1), the shale gas will take up nearly half of the traditional gas supply by 2040. With the huge available resources and growing energy demand, Shale reservoir has recently received significant interest and investigations. To optimize the recovery of unconventional reservoirs, further technology advancement is needed to face and deal with some technical challenges from the pore scale to the field scale, such as deep water, high temperature and high pressure, and complicated reservoir conditions.

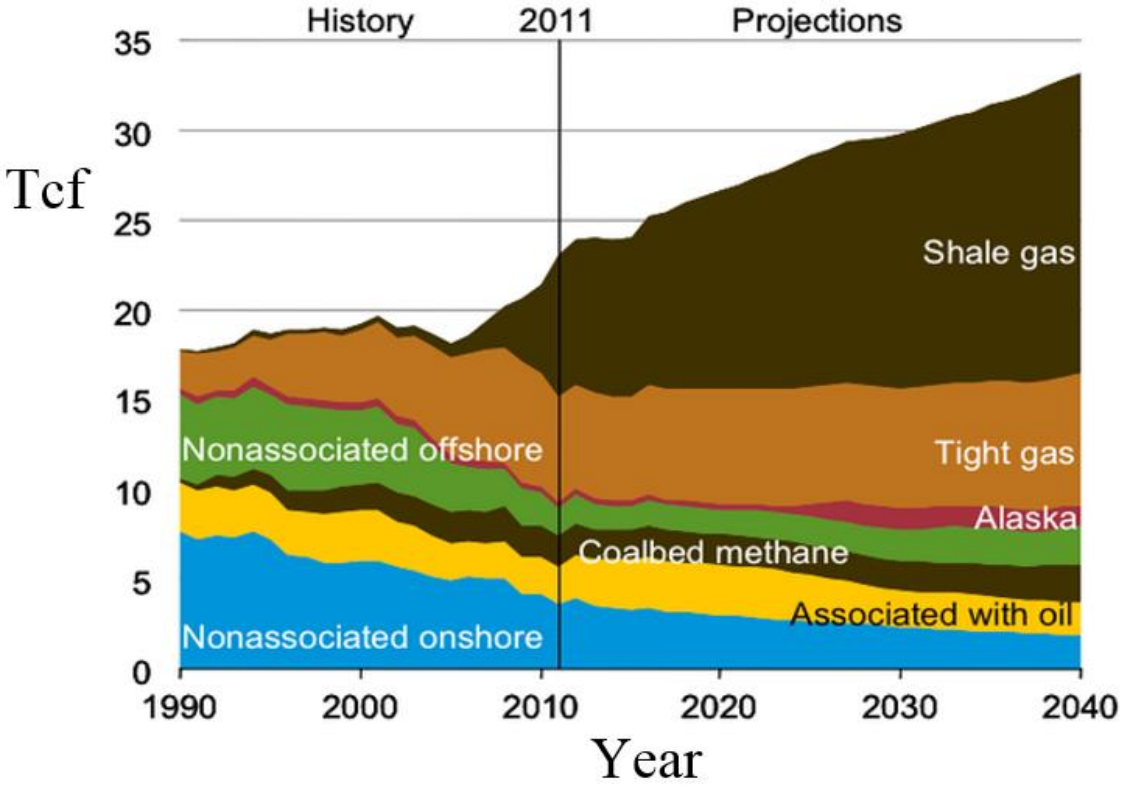

Figure 1: U.S. dry natural gas production (Tcf/year, EIA: Annual Energy Outlook 2013).

Existing technologies are unable to provide accurate results locating and characterizing the hydrocarbon in place for these reservoir conditions mentioned above. The oil industry still relies on downhole electrical and electromagnetic imaging methods to improve the characterization and understanding of reservoirs, while conventional electrical sensors and measuring may not work well in high temperature and high pressure conditions. Also chemical EOR process including polymer or surfactant flooding and alkaline injection are limited by high costs, potential corrosion and fluid loss (Kong and Ohadi, 2010). Currently, Development of nanotechnology has successful offered technically and economically feasible alternatives for materials and technologies in many industries. Introduced by Feynman in 1959, nanotechnology was a great idea to exactly manipulate atoms and molecules and to create nanoscale machines at one dimension size from 1 to 100 nanometers. To give a better visualization about nano scale, Figure 2 shows the length scale from millimeter to nanometer. Because of tiny size of nanoparticles, gravity becomes negligible while both wan der Waals attraction and surface tension become important. With those advance revolution and potential advantages, application of nanoparticles have also attracted much attention and displayed numerous potential to lead evolutionary changes in petroleum industry, such as enhanced oil recovery, nano- scale sensors, improving downhole separation, aiding in the development of non-corrosive materials, improving the drilling and completion process, and so on. For instance, nanotubes could be applied to create lighter, stronger, and more corrosion-resistant structural materials in platforms for offshore drilling (Esmaeili, 2009). In a word, numerous areas about nanotechnology could contribute to

more-efficient, less expensive, and more-environmentally sound technologies in oil & gas industry (Matteo et al. 2012).

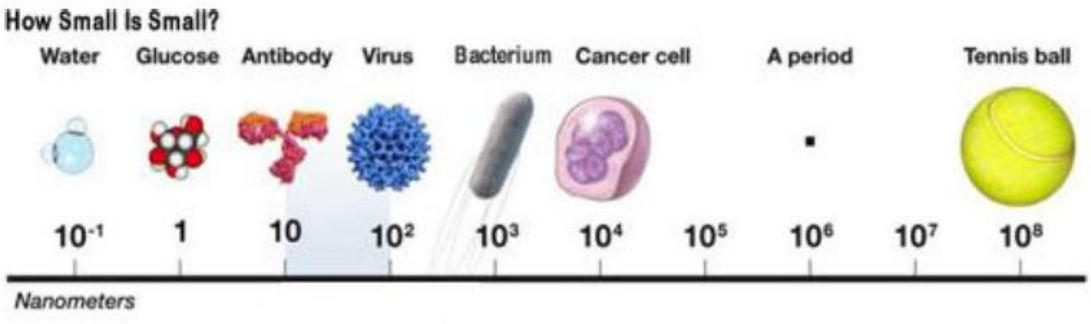

Figure 2: Length scale from millimeter to nanometer (Davis, 2009).

Nuclear Magnetic resonance (NMR) is widely used in petroleum industry for petrophysical laboratory research and subsequently developed downhole logging tool for in-situ reservoir evaluation. Nuclear magnetic resonance (NMR) logging is a type of well logging that uses the NMR response of a formation to directly determine its porosity and permeability, and provide a continuous record along the length of the borehole. Because NMR logging measures the induced magnet moment of hydrogen nuclei (protons) which are contained in the fluid-filled pore space of porous media, it could effectively responds to the volume, composition, viscosity, and distribution of these fluids.

Atomic nuclei spin and this angular moment produces a magnetic moment. The NMR measures the magnetic signal which is emitted by spinning hydrogen nuclei as they return to their original state following stimulation by an applied magnetic field and pulsed radio frequency energy (PetroWiki, NMR). NMR devices apply strong magnets

to create a static magnetic field which could aligns the protons in the pore fluid from their random state to the direction of the imposed magnetic field. The hydrogen nuclei behave as though they are tiny bar magnets aligned with the spin axes of the nuclei because of their inherent nuclear magnetism on Figure 3. In the absence of an external magnetic field, the nuclear magnetic axes are randomly aligned. Therefore, the NMR signal amplitude is proportional to the quantity of hydrogen nuclei present in the formation and external magnetic matter.

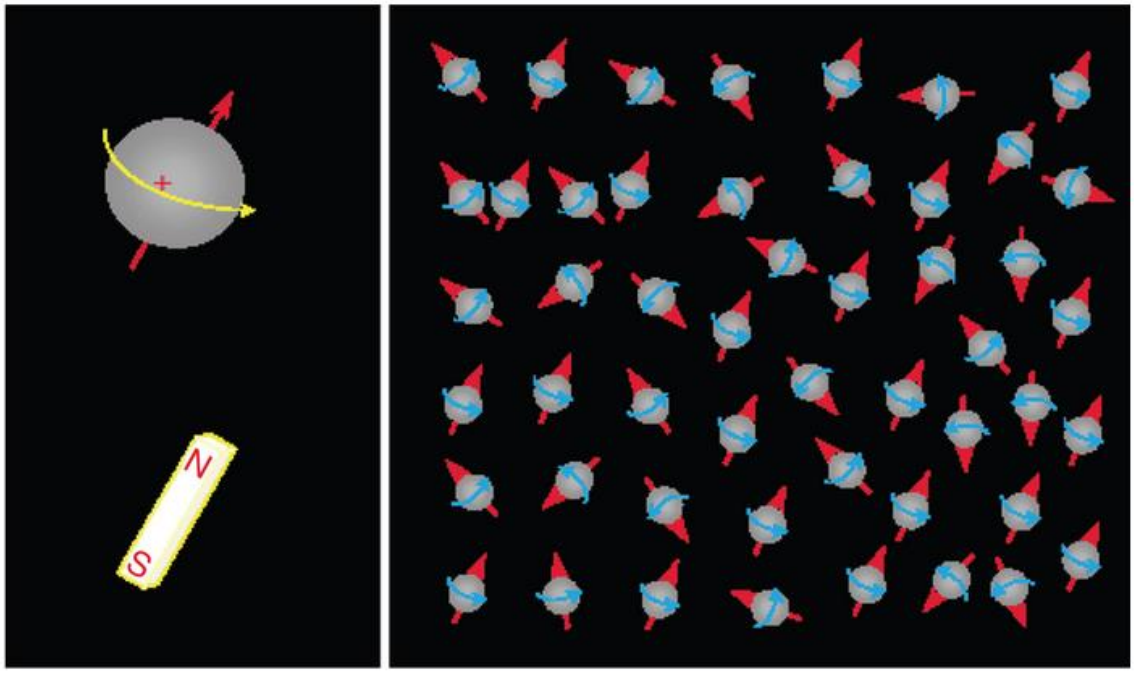

Figure 3: The distribution of hydrogen nuclei with and without an external magnetic field (PetroWiki).

Shale reservoirs are fine grained sediments with low porosity and extremely low permeability, which are both the source rock and the reservoirs (Javadpour, 2009).

Hydraulic fracturing and horizontal drilling are two necessary technologies to make shale gas becomes commercial producing. The success of the Barnett shale has proved that gas could be economically produced from source rock, not reservoir rock. This revelation has resulted in the exploration and development of many other shale gas reservoirs, such as the Woodford, Fayetteville, Marcellus, and the Haynesyille on the Figure 4. Wang and Reed (2009) and Sondergeld et al. (2010) proposed that the organic-rich shale reservoirs contains four pore systems: hydrophobic pores in the organics matter, pores of indeterminate wettability in the non-organic part of matrix, natural fractures most likely dominantly water wet, and stimulation produced fractures that possibly have fractional wettability. Dark objects are kerogen and the smaller darker objects within the kerogen are pores on the Figure 5. Larger silt grains are mixed in the flow structures in the upper portion of the Figure 5. Due to the organics can store methane as adsorbed gas and absorbed gas, shale gas is usually considered to exist in three forms: compressed gas in pores and fissures, adsorbed gas in the organic and inorganic matter, and dissolved gas in the kerogen (Javadpour 2009; Zhang et al. 2012). Meanwhile, taking into account of extremely low permeability and the micro and nano-

scale of pore, some non-Darican mechanisms including gas diffusion, desorption and slippage flow have been considered to better explain the gas transport in shale reservoirs (Civan et al. 2011; Shabro et al. 2012; Cipolla et al. 2009; Swami 2012; Swami and Settari 2012).

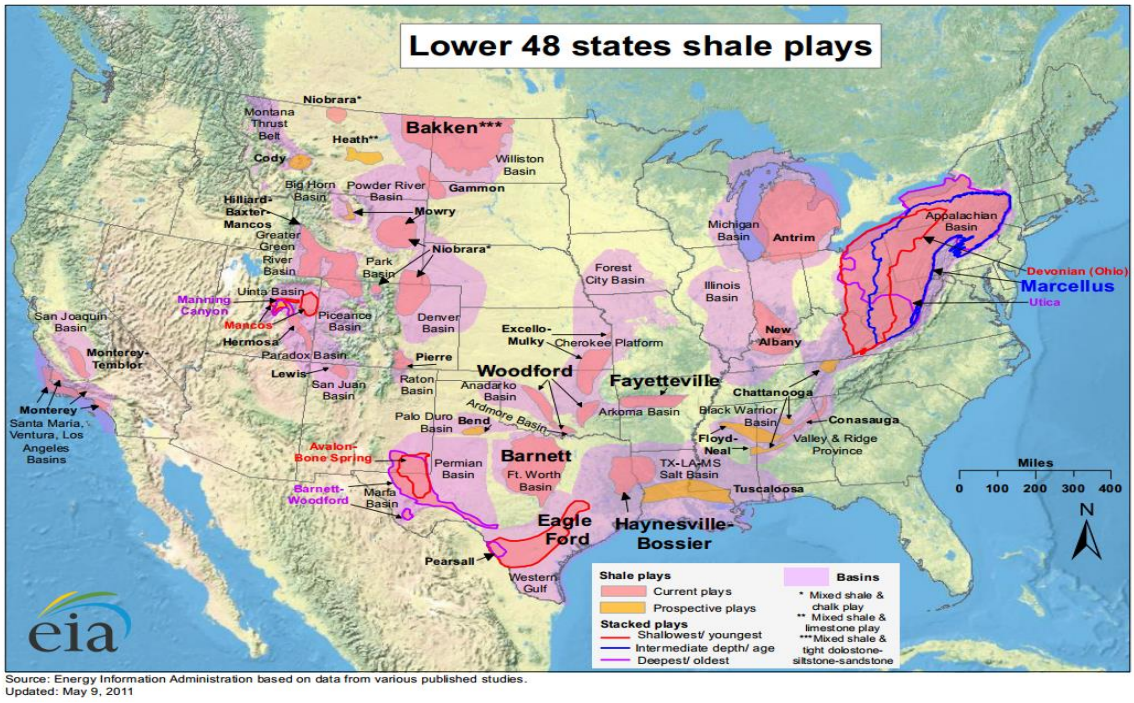

Figure 4: Lower 48 Shale gas plays (Energy Information Administration, 2011).

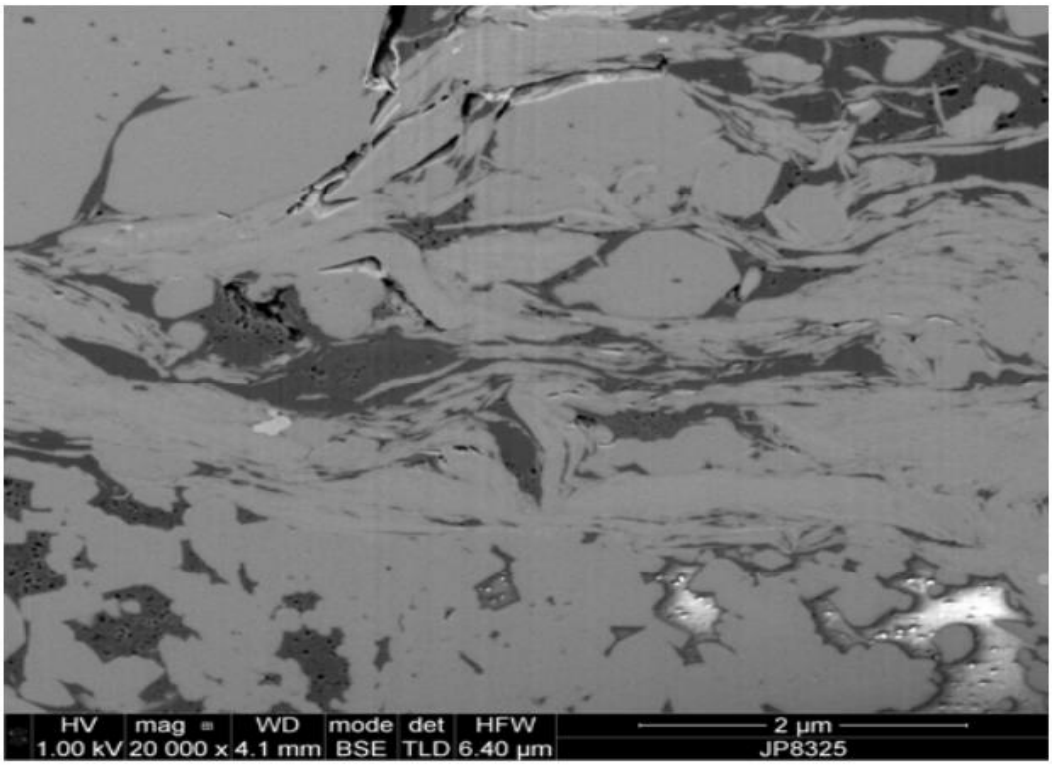

Figure 5: SEM image of an ion-milled Barnett shale sample including kerogen, pores space and clay platelets (Sondergeld et al., 2010).

Due to various flow mechanism, many innovative methods have been proposed to describe the flow process in tight formations. The Dual-Mechanism Approach, Darcy flow and Fickian diffusion occur parallel in matrix, was introduced to characterize the gas flow in coal or shale formations through the dynamic gas slippage factor (Clarkson, et al., 2010). The apparent permeability considering Knudsen diffusion, slippage flow and advection flow was brought forward for the pore scale modeling by Javadpour (2009). Based on the unified Hagen-Poiseuille-type formula, Civan et al. (2010) proposed a technique to calculate apparent permeability through the flow condition function and the intrinsic permeability of porous medium. However, these models don

not provide clear and proper connectivity between different pore systems. Yan et al. (2013a and 2013b) and Alfi et al. (2014) have established a micro scale multiple porosity model for fluid flow in shale reservoirs, which divides the reservoirs into three separate porosity systems: organic matter, inorganic matter, and natural fractures. They have also built up a two phase micro model in where mixed wettability, high capillary pressure and the kerogen randomly distributed are brought in to interpret the dynamic of gas and water flow at this micro scale level (Yan et al. 2013c).

Fracture direction is most influenced by the formation stresses, while it could be also be modified by the fracture design, such as the treatment pressure and volume. Typically, multiple transverse hydraulic fractures are created if the wellbore is design and drilled in the direction of minimum horizontal stress (Bartko et al. 2013). Hydraulic fracture is one of necessary techniques to produce oil & gas from extra-low permeability reservoir. In conventional reservoirs and tight gas sands, single plane fracture half-length and conductivity are the key parameters to describe stimulation performance. However, Fisher et al. (2002) stated microseismic images from the Barnett shale showed significantly more complex network structures than typical patterns in tight gas sands, so the concepts of single-fracture half-length and conductivity are insufficient to describe stimulation performance. The concept of stimulated reservoir volume (SRV) was developed by Fisher at al. (2004) to provide some quantitative measure of stimulation effectiveness in the Barnett shale based on the size of the microseismic images (Mayerhofer et al. 2010). Their work also presented that production is related directly to the reservoir volume stimulated during the fracture treatments. Various types of fracture

growth including simple fractures and complex fracture network are display in Figure 6. Secondary fractures are often generated along with the changed condition of the fracture design, which in return increases the area of the flow path and fracture conductivity. Moreover, some secondary fractures have been found in micro-seismic events and outcrops. King et al. (2008) presented a good example in Figure 7, which is the micro-seismic captured from simultaneously fractured well. Complex-fracture networks could improve the fracture surface contact area with the shale through both size and fracture space.

SRV derived from microseismic data could assistant reservoir modeling with fractures and supply a measure of overall hydraulic fracture performance. Maximizing the total SRV plays a critical role in the successful economical production from the unconventional gas reservoirs, because it could increase the fractures conductivity and speed up the gas and liquid flow (Yu and Sepehrnoori 2013). In addition, the gas flow process from the ultralow permeability rock to the complex fracture network should be modeled to effectively evaluate stimulation design and completion strategies. Consequently, the complex fracture network and primary hydraulic fracture would be better discretely characterized to achieve the modeling results mentioned above.

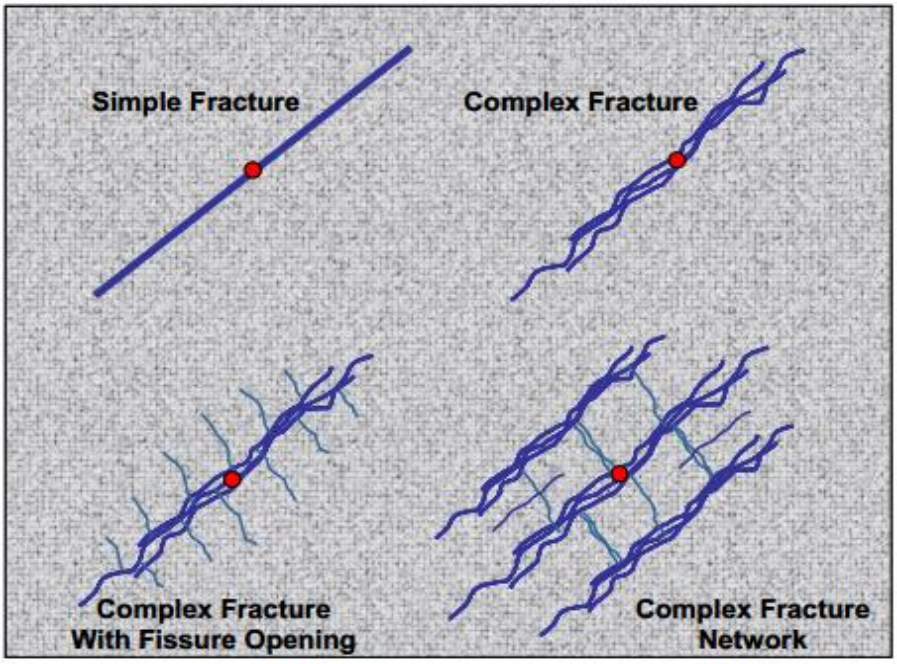

Figure 6: Types of fractures growth (Warpinski et al. 2008).

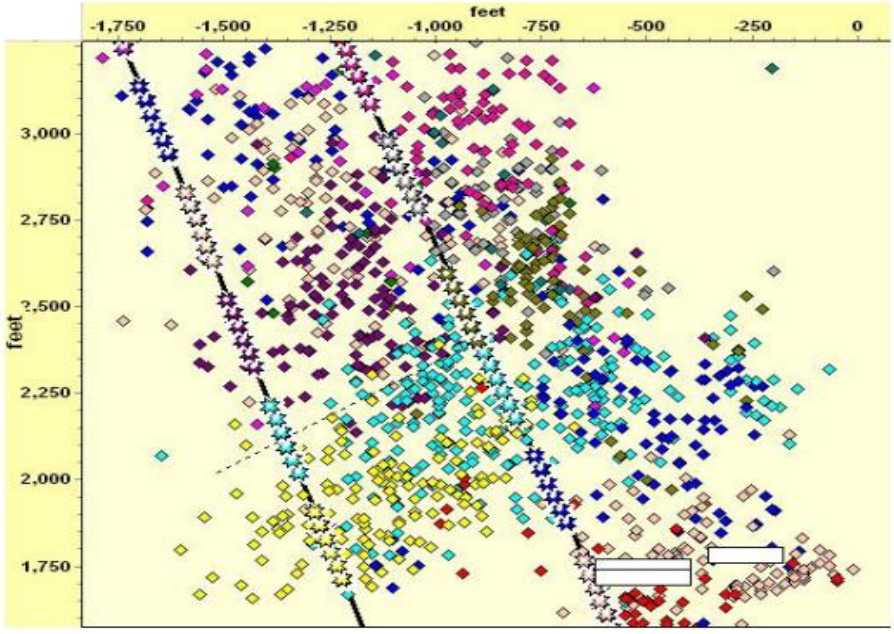

Figure 7: Microseismic record of fracturing events. (King et al., 2008)

Magnetic nanoparticles are a class of nanoparticles which could be manipulated using magnetic field and commonly consist of iron and their chemical compounds. Magnetic nanoparticles are of great interest of researchers from a wide range of disciplines including magnetic fluids, catalysis, biotechnology or biomedicine, magnetic resonance imaging, data storage, and environmental remediation. The physical and chemical properties of magnetic nanoparticles largely depend on the synthesis method and chemical structure. In most case, the particles range from 1 to 100 nm in size and may present some superparamagnetism. Ferrite nanoparticles are the most explored magnetic nanoparticles. Ferrite particles smaller than 128 nm become superparamagnetic, which prevents self-agglomeration since they exhibit their magnetic behavior only when an external magnetic field is applied.

In spite of many applications of nanoparticles accomplished in petroleum industry, complex reservoir conditions such as high salinity, low permeability and porosity, and heterogeneous rock properties, still make nanotechnology challenging. The study of nanoparticles transport in porous medium is one critical issue for both environmental concern and reservoir application (Wu and Pruess 2000; Yu et al. 2010). Few works have been completed to address the issue related to mathematical and numerical modeling of nanoparticles transport in porous medium. Ju et al. (2009) and Sbai et al. (2011) established a mathematical model of nanoparticles transport in two-phase flow in porous media based on the formulation of fine particles transport. El-Amin et al. (2012) also introduced a reservoir model to simulate the nanoparticles transport in porous media where mixed relative permeability, mixed-wet system and variations of

both porosity and permeability are considered and contained. Yu (2012) conducted many core-flooding experiments to test the distribution of nanoparticles in cores samples and also obtained the quantitative measurement looking at the mechanism of nanoparticles transport in porous media. Zhang (2012) performed numerical simulations to compare results with the results from core-flooding experiments, and also discussed and analyzed the interactions between particles and rock surface. Kai et al. (2014) built a two-phase fluid flow simulator for transport of injected nanoparticles in homogenous and heterogeneous rock, and also compared their numerous results with the results from their core-flooding experiments.

To our knowledge, little work has been conducted of the nanoparticle transport in unconventional reservoirs such as shales. The nanoparticle diameters are normally 1 to 500 nm, which means Brownian diffusion must be considered in the model. Moreover, various components of shale and complicated local flow mechanisms make modeling nanoparticles transport in shale reservoir more challenging. Therefore, an accurate mathematic model is required for better interpreting the transport process of particles based on the various flow physics and the interactions among different porous media.

1.3 Objective and Procedures

The objective of this research was to build a mathematical model for simulating the nanoparticle transport in shale reservoirs, where the dynamic flow of water and gas could be clearly characterized. Darcy flow, Brownian diffusion, gas diffusion and desorption, slippage flow, and Capillary effect were incorporated in this simulator. Moreover, these diverse mechanisms mentioned above are separately applied to different media because of various media properties. In addition, the water saturation, mass concentration of nanoparticles, grid pressure, and the magnetization of reservoir could be computed and displayed for both micro and macro models including reservoir stimulated volume. The sensitivity analysis could be also conducted to investigate the effect of nanoparticles size, strength of magnetism of nanoparticles, Darcy flow, Brownian diffusion, capillary pressure, and SRV patterns on the results.

To achieve the above objective and obtain the expected results, we built a reservoir model looking at nanoparticles transport in water-gas phase in shale porous medium. Six main tasks were performed.

Task 1: Build a mathematic model to mimic nanoparticle transport in hydraulic fractures and natural fractures where convection flow and Brownian diffusion physics are considered. Three mass balance equations for water, gas and nanoparticles are applied to solve the unknown variables by using Newton-Raphson iteration.

Task 2: Develop a micro model looking at nanoparticles' transport in water-gas phases in shale matrix containing inorganic matter and organic matter. Organic matter is randomly distributed among the matrix and acts as hydrocarbon-wet phase. The water

flow is mainly governed by the Darcy law while the gas flow behaves differently because of extremely low permeability and micro and nano-scale of pores. Besides, nanoparticles only transport in the aqueous phase which means it cannot flow into the gaseous phase. The interaction between colloids and reservoir matrix is ignored.

Task 3: Perform the simulator for the 1D micro model, 2D micro and macro models, and 3D reservoir models. The 1D micro model could clearly show how does water phase flow into the matrix and the change trend of water saturation and concentration of nanoparticles. The 2D micro models include 12×12 grids and the size of each grid for X, Y, and Z are $1 \times 10^{-5}\ m, 1 \times 10^{-5}\ m, and\ 1 \times 10^{-5}\ m$. The distribution of water saturation and nanoparticles concentrations at different time steps in the 2D micro and macro models with and without organic matter are displayed. The 3D reservoir mode is one good numerical case to show the dynamic flow in three dimensions, just like the real reservoirs. In addition, to obtain the more accurate results and validate them, we refine the mesh grids and perform the simulator again for the 2D models. The results will be compared with that of previous non-refine models.

Task 4: Conduct the simulator for the 2D reservoir models including various SRV patterns and compute and obtain the distribution of nanoparticles concentration and magnetization of reservoirs. A stimulated reservoir area has been selected to represent the fractured shale reservoir in our model. Since the partial objectives of this research is to verify the magnetic nanoparticles could effectively enhance signals from well logging devices, the total magnetization of reservoir is computed and presented. We will check and compare the signal from the numerical cases with and without the magnetic

nanoparticles. Cheng et al. (2014) have conducted some magnetic susceptibility experiments to investigate the influences of magnetic nanoparticles, so our numerous results will be also compared with their experiment data.

Task 5: The effects of nanoparticles size, strength of magnetism of nanoparticles, Darcy flow, Brownian diffusion, capillary pressure, and SRV patterns are separately analyzed for better understanding the function of these corresponding parameters. Firstly, the base numerous case is conducted to acquire the results. Secondly, the compared cases where only the sensitized factor varies and all other inputs keep the same, are performed at the same initial condition. Lastly, the two results are compared and analyzed to explain how these factors affect the flow process and distribution of magnetization.

Task 6: Perform numerical simulations to match logging results if some field data are available, update flow mechanism and some corresponding parameters and determine model predictability.

1.4 Organization of Thesis

As the same with table of content, this thesis is mainly divided into four chapters, which are organized and described as below:

1) Chapter I firstly brings out the research questions and then introduces the background and some literature review about this research topic. Next the objective of this research and some main procedures are shown.
2) Chapter II focuses on the models description, which include the mathematical model, 1D micro model, 2D micro and macro models, and large reservoir model. Moreover, the magnetism analysis is also introduced and explained.
3) Chapter III mainly shows, explains and discusses the numerical results from these models above. In addition, the results from the magnetism analysis are also displayed to validate the accuracy of this simulator.
4) Chapter IV sums up all the data and results and presents some major significant conclusions.

CHAPTER II

MODELS DESCRIPTION

2.1 Introduction

In this chapter, firstly a mathematical model has been introduced and developed to describe the nanoparticles transport in two phases (aqueous and gaseous) in shale reservoirs. The aqueous phase contains water and nanoparticles and the gaseous phase includes natural gas methane. Secondly, various numerical models including 1D model, 2D micro and macro modes, 3D model are built and described, where inorganic matter, organic matter, and fractures are different separate media to analyze. Thirdly, a large reservoir model including reservoir stimulating volume and wellbore has been developed, which could fully model how does nanoparticles flow from the wellbore to the fractures and matrix.

With the advantages of advanced analytical tools, such as SEM, kerogen matter has been found to be widely scattered in many shale matrix, such as Eagle Ford, Woodland, and Bakken. Moreover, the presence of kerogen could provide more available hydrocarbon sources, improve matrix porosity, alter grain density and wettability, and bring in various flow mechanisms in shale reservoirs (Curtis et al. 2010 and Ambrose et al. 2010). Figure 8 displays smaller pores reside on the wall of large pores in kerogen, and Figure 9 shows the kerogen network in the 3D SEM images. As we discussed above, the shale reservoirs usually contain organic matter, inorganic matter, and fractures, so to subdivide the shale matrix into the inorganic matrix and the

organic matrix with different pore geometries could better describe and explain the diverse connections and capture different flow mechanisms between various pore systems. Characterized as high permeability, natural fractures act as pathways to connect shale matrix blocks with the induced fractures network or the well bore. Besides, for all the numerical models in this paper, the kerogen matter is randomly distributed in the matrix and their abundance is directly related to the properties of each medium and the Total Organic Carbon (TOC) content in the Equation (1) (Yan et al. 2013). The inorganic matter is water-wet while the kerogen matter is considered to be hydrocarbon-wet, which could produce a difference of capillary pressure and relative permeability on various pore medium. For example, the water mobile pressure is smaller to its grid pressure in the inorganic matter because of capillary pressure, while it is equal to its grid pressure in the kerogen matter.

$$TOC = \frac{\rho_{krg} N_{krg} (1-\phi_{krg})}{\rho_{krg} N_{krg} (1-\phi_{krg}) + \rho_{inorg} N_{inorg} (1-\phi_{inorg})} \times 100\ wt\% \quad (1)$$

Where ρ_{krg} denotes the density of the kerogen matter, N_{krg} denotes the number of kerogen grids in the mesh, ϕ_{krg} denotes the porosity of the kerogen matter in the shale matrix, ρ_{inorg} denotes the density of the inorganic matter, N_{inorg} denotes the number of inorganic grids in the mesh, ϕ_{inorg} denotes the porosity of the inorganic matter in the shale matrix.

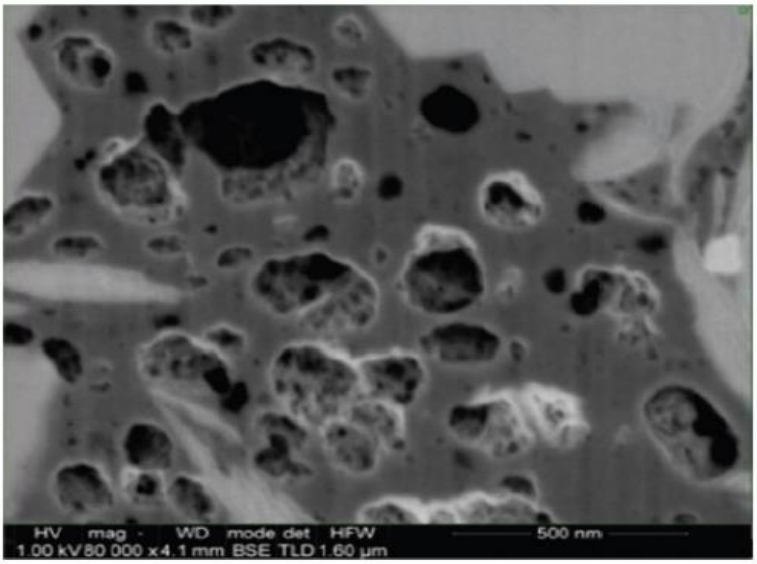

Figure 8: Local pore distribution in kerogen, smaller pores reside on the wall of large pores (Curtis et al. 2010).

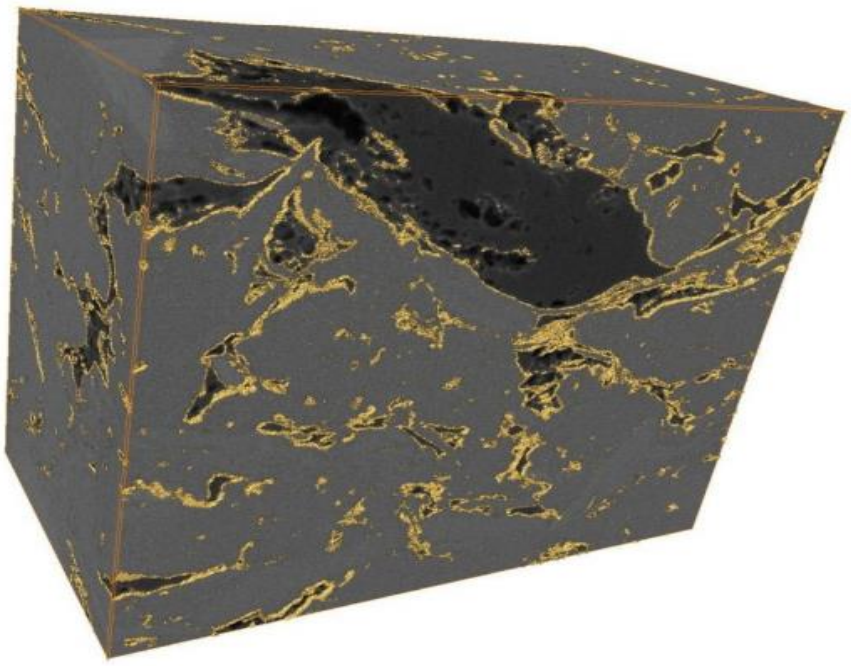

Figure 9: 3D SEM segmentation showing kerogen network, yellow outlines the kerogen network (Ambrose et al. 2010).

In our numerical simulator, two phases flow carrying nanoparticles will be modeled in different pores systems. As the mean free path of gas molecules becomes enough small, the interaction between molecules and rock surface will play a very important effect in addition to the viscous flow. Diffusive flow has to be considered based on the micro-scale and nano-scale pore size. Bird et al. (2007) stated the gas transport mechanisms in fine porous media are made up with Knudsen diffusion, viscous convection, and slip flow. Figure 10 presents the flow mechanisms of gas flow in the nano pores of shale strata. Red molecules represent Knudsen diffusion, deep green molecules stand for slip flow, and deep orange molecules represent viscous flow. Different with conventional gas reservoirs, the gas storage mechanism is involved with compressed gas and adsorbed gas. As reservoir pressure decreases, adsorbed gas in the kerogen will be gradually desorbed as free gas which will flow out into the fractures. The gas desorption actually increases the gas accumulation in kerogen matter.

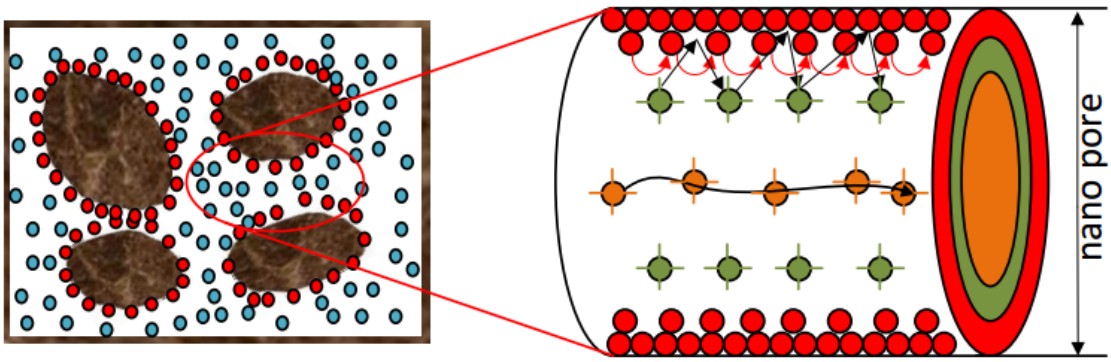

Figure 10: Gas flow mechanisms in matrix nano pores. (Guo et al. 2014).

In addition to gas storage mechanisms and fluid flow, capillary pressure, relative permeability and wettability in the organic shale reservoirs are more complicated than typical conventional reservoirs. Capillary pressure effect will become significant for the tiny pore size in the shale matrix. Since kerogen matters are considered to be gas wet and inorganic matters are regarded as water wet in our models, water could be layered on the grain surface in the inorganic matter and gas could flow in a continuous phase. Based on the similarities in mineralogy and petrophysical properties of the shale and sand type reservoirs, the Brooks and Corey formulation is applied for capillary pressure calculations as following (Brook and Corey, 1964). Based on the formulations, Figure 11 shows the capillary pressure curves used in our numerical models. Figure 12 presents two phases' relative permeability curves along with the changing of wetting phase saturation.

$$S_e = \left(\frac{P_e}{P_c}\right)^{\lambda} \tag{2}$$

$$S_e = \frac{S_w - S_{wr}}{1 - S_{wr}} \tag{3}$$

Where S_e is effective water saturation, P_e is the capillary entry pressure, P_c is the capillary pressure at a wetting phase saturation S_w, and S_{wr} is the residual wetting phase saturation.

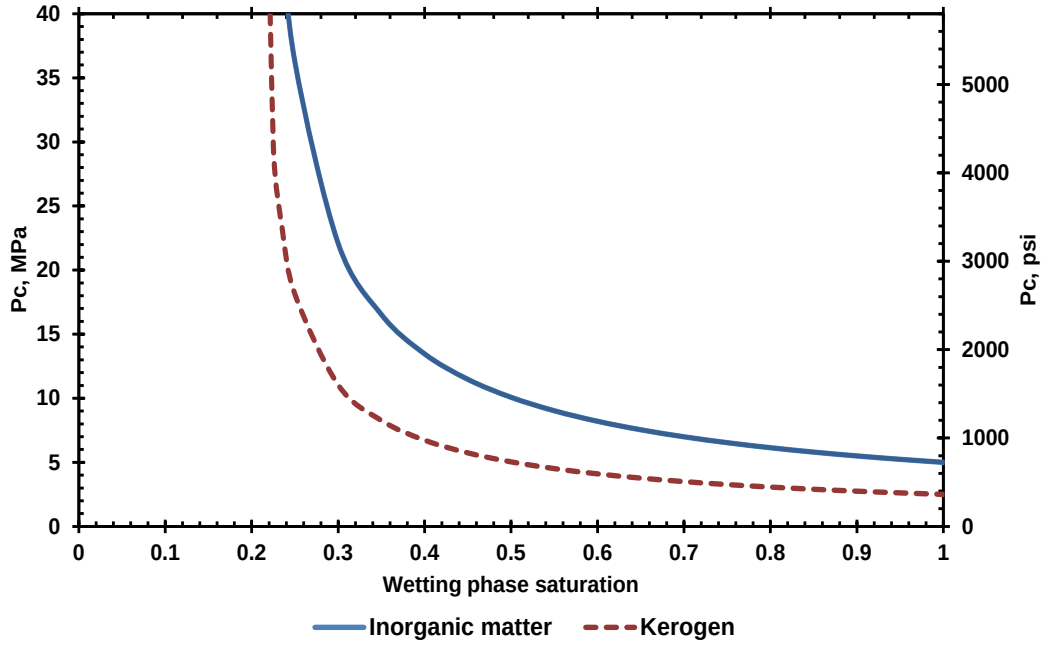

Figure 11: Capillary pressure vs. wetting phase saturation for Inorganic matter and Kerogen matter.

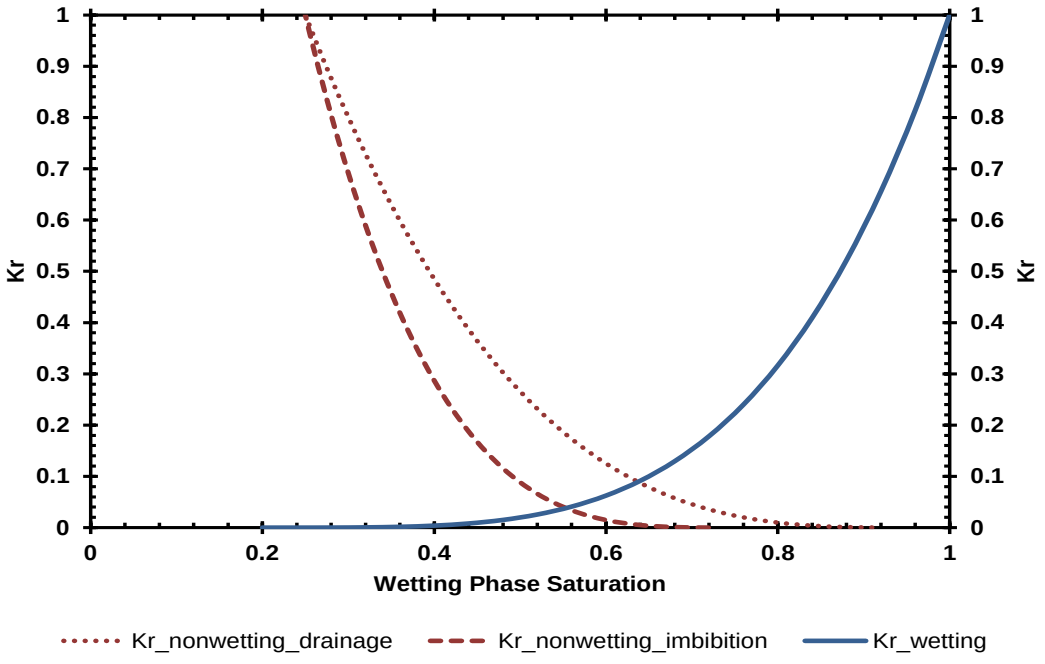

Figure 12: Relative permeability curves applied for our numerical models.

Since we are cooperating this project with Dr. Zoya Heidari's petrophysical group, so the nanoparticles we used in our model is almost same with their experiments. As Cheng et al. (2014) stated that, the iron oxide nanoparticles are produced by the reaction of hydrogen peroxide with ferrocene dissolved in acetone with the solvothermal chemical approach. In addition, with the negative charged, these nanoparticles are capable of electrostatic repulsion to prevent the deposition in the pore space.

2.2 Mathematical Model

A mathematical model looking at the nanoparticles transport in two phases is introduced below. The water flow is mainly governed by the Darcy law, while the gas flow behaves differently because of extremely low permeability and micro and nano-scale of pores. Based on the Darcy equation, gas diffusion, gas desorption and slippage flow are also considered to explain the gas transport in shale reservoirs. Since the nanoparticles size used in this paper is about 30-80 nm which is small enough to perform strong Brownian motion, convection flow and Brownian diffusion are two major contributor for its transport. In order to study the transport mechanism of nanoparticles in fractured tight reservoirs, some assumptions are proposed to simplify and assistant the understanding of the complicated flow in shale reservoirs.

(1) Nanoparticles only transport in aqueous phase.

(2) Nanoparticle deposition is not significant and the interaction between colloids and matrix is ignored.

(3) Shale rock is comprised of inorganic matter, organic matter, inter/intra-granular pore space, and natural fractures.

Three main mass balance equations for water, gas and nanoparticles, are applied to solve the unknown variable with the effective Newton-Raphson iteration in this simulator as below. All the numerical cases are performed in isothermal environment in this paper, so the heat balance equation is neglected.

$$\frac{\partial}{\partial t} M_l = \nabla \cdot \left(\overrightarrow{F_l}\right) + \sum Q_l \tag{4}$$

$$\frac{\partial(\phi S_w C)}{\partial t} + \nabla \cdot (C\overrightarrow{v_w}) = \nabla \cdot (D_e \nabla C) + \sum Q_{Nano} \tag{5}$$

Where l is the index of component, water or gas, M is the mass accumulation of component l, F is the flux of component l, Q is source/sink of component l, C is concentration of nanoparticles, Q_{Nano} is the source/sink of nanoparticles, D_e is the diffusion coefficient of nanoparticles which is obtained from the modification of stokes-Einstein's equation (Millington and Quirk 1961; Elimelech and O'Melia 1990).

To better explain these mass balance equation (4) and (5) above, another equations with more detail are presented as below.

$$M^l = \sum_\beta \phi S_\beta \rho_\beta X_\beta^l \tag{6}$$

$$\overrightarrow{F_A}^l = -\rho_A k \frac{k_{rA}}{\mu_A} (\nabla P + P_c - \rho_A \vec{g}) X_\beta^l \tag{7}$$

$$\overrightarrow{F_G^l} = -\rho_G k \frac{k_{rG}}{\mu_G}(1 + \frac{b}{P})(\nabla P + P_c - \rho_G \vec{g}) X_\beta^l \quad (8)$$

$$D_e = \frac{K_b T}{3\pi\mu d_p} \phi^{\frac{3}{4}} S_w^{\frac{10}{3}} \quad (9)$$

Where β is the index of fluid phase (A is aqueous phase and G is gaseous phase), ϕ is the porosity of porous media, S_β is the saturation of phase β, ρ_β is the density of phase β, X_β^l is the mass fraction of component l in the phase β, k is the absolute permeability of porous media, k_{rA} is the relative permeability to the phase β, μ_β is the viscosity of phase β, P_c is the capillary pressure, b is the Klinkenberg factor accounting for gas slippage effects, K_b is the Boltzman constant, T is the absolute temperature, d_p is the diameter of nanoparticles.

These continuum equations are discretized in space using the integral finite difference method. On the Figure 13 below, two grid block m and n share with the interface A_{nm}. V_m and V_n are the volume of grid m and n, and d_m and d_n are the distance from the center point to the interface, respectively. F_{nm} is the average value of normal flux from grid m to grid n.

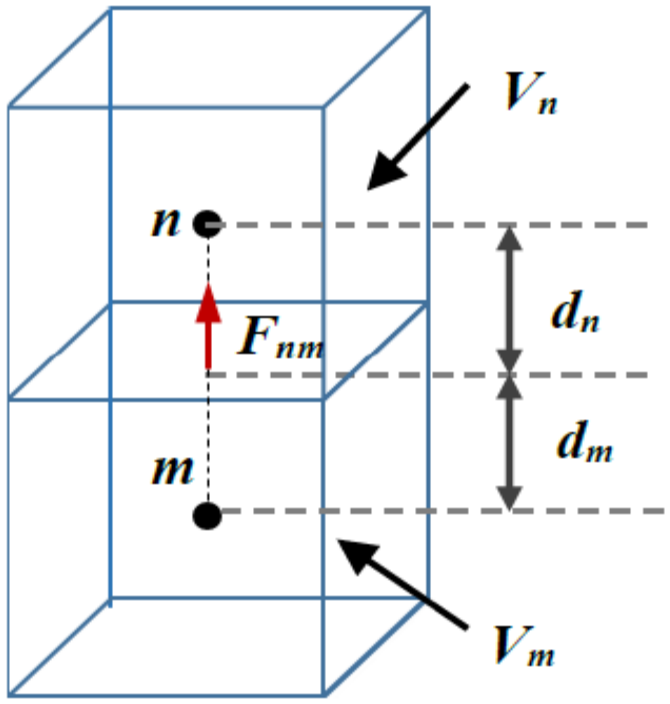

Figure 13: Space discretization and geometry parameters in the integral finite difference method (Kai et al. 2014).

After introducing appropriate volume averages, the accumulation term changed as Equation (10), and the flux term also varied as Equation (11). The discretized flux could be expressed in terms of averages over parameters for grids V_m and V_n, so the Darcy flux term could be also changed as Equation (12).

$$\int_{V_n} M^k \, dV = V_n M_n \tag{10}$$

$$\int_{\Gamma_n} \boldsymbol{F}^k \bullet \boldsymbol{n} d\Gamma = \sum_m A_{nm} F_{nm}^k \tag{11}$$

$$F_{nm}^{k} = -\rho_A k_{nm} \frac{k_{rA}}{\mu_A} \left(\frac{P_n - P_m}{d_{nm}} + P_c - \rho_A g_{nm} \right) X_A^k$$

$$-\rho_G k_{nm} \frac{k_{rG}}{\mu_G} (1 + \frac{b}{P_{nm}}) \left(\frac{P_n - P_m}{d_{nm}} + P_c - \rho_G g_{nm} \right) X_G^k \quad (12)$$

$$D_{nm} = D_m + D_n \quad (13)$$

Where M is a volume-normalized extensive quantity, and M_n is the average value of M over V_n, F_{nm} is the average value of the inward normal component of $\vec{\boldsymbol{F}}$ over the surface segment A_{nm} between volume grids V_m and V_n, the subscripts (nm) denote a suitable averaging at the interface between grid blocks m and n, g_{nm} is the component of gravitational acceleration in the direction from m to n.

Substituting Equations (10), (11) and (12) into the governing Equation (1), a set of first-order ordinary differential equations in time is obtained, as expressed on Equation (14). Using the fully implicit, time is discretized as a first-order finite difference and the flux and sink and source terms are evaluated at the new time level, $t + 1 = t + \Delta t$. The time discretization results in a set of new coupled non-linear, algebraic equations on Equation (15).

$$V_n \frac{dM_n^k}{dt} = \sum_m A_{nm} F_{nm}^k + q_n^k \quad (14)$$

$$R_n^{k,t+1} = M_n^{k,t+1} - M_n^{k,t} - \frac{\Delta t}{V_n} \left(\sum_m A_{nm} F_{nm}^{k,t+1} + V_n q_n^{k,t+1} \right) = 0 \quad (15)$$

where $R_n^{k,t+1}$ is residuals, superscript k is component index (water, gas, or nanoparticles), superscript t represents the previous time step, $t+1$ stands for the current time step.

For each volume element (grid block) V_n, we have N_k equations. If the mesh contains N_E gird blocks, Equation (15) stands for a total of $N_k \times N_E$ coupled non-linear equations. The unknown equations including $N_k \times N_E$ independent primary variables are solved by Newton Raphson iteration. The Taylor series of the residual is given as Equation (16). Retaining only terms up to first order, the increments $(x_{i,p+1} - x_{i,p})$ could be computed from a set of $N_k \times N_E$ linear equations as Equation (17).

$$R_n^{k,t+1}(x_{i,p+1}) = R_n^{k,t+1}(x_{i,p}) + \sum_i \frac{\partial R_n^{k,t+1}}{\partial x_i} \left| (x_{i,p+1} - x_{i,p}) + \ \ldots = 0 \right. \tag{16}$$

$$-\sum_i \frac{\partial R_n^{k,t+1}}{\partial x_i} \left| (x_{i,p+1} - x_{i,p}) = R_n^{k,t+1}(x_{i,p}) \right. \tag{17}$$

All terms $\partial R_n / \partial x_i$ in the Jacobian matrix are evaluated by numerical differentiation. Iteration is continued until the residuals $R_n^{k,t+1}$ are reduced below a present convergence tolerance, relative convergence criterion or absolute convergence criterion. If convergence cannot be achieved within a certain number of iterations, the time step size Δt will be reduced and a new iteration process is started. The space and time discretization and the Newton Raphson Iteration techniques are referenced from Moridis and Pruess (2008).

2.3 1D Micro Model

To clearly investigate and explain the flow process of nanoparticles carried by water and gas phases, the easiest 1D micro model has been built. The 1D micro model contains 20 grids: two sides of grids representing for natural fractures and the other middle eighteen grids stand for non-organic matter. As the Figure 14 below, grids 'I' are natural fractures grids representing inactive block, which means its pressure, water saturation, and all others properties keep the same. The mesh for 1D model is $20 \times 1 \times 1$ grids and the size of each grid for X, Y and Z are $1 \times 10^{-5}m, 1 \times 10^{-5}m, 1 \times 10^{-5}m$. The main parameters for the fractures and non-organic matter are shown on the Table 1. The fracture media has the higher permeability, higher water saturation and higher mass concentration of nanoparticles than the middle non-organic grids. The porosity of inorganic matter of shale matrix is very small, only 0.02, and we don't consider the diffusivity effect for the fracture and inorganic medium. Due to the left fracture grid has higher pressure, $2.72 \times 10^7\ Pa$ than the middle grids, $1.72 \times 10^7\ Pa$, and the middle grids have larger pressure than the right fracture gird, $0.72 \times 10^7\ Pa$, so the flow direction is from left side to right side. In addition, the temperature will keep constant, so the model will be performed under the isothermal status.

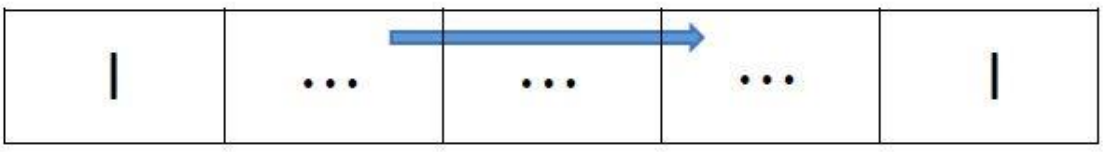

Figure 14: Mesh scheme for 1D model.

Table 1: Main parameters of the pore medium for the 1D model

Pore Medium	Fracture	Inorganic
Density, $kg/m3$	--	2.6×10^3
Porosity	1.0	0.02
Permeability	84 mD	50 nD
Diffusivity, m^2/s	--	--
Pressure, Pa	$2.72 \times 10^7, 0.72 \times 10^7$	1.72×10^7
Water Saturation	0.99	0.21
NPs Concentration, kg/L	$1.0 \times 10^{-6}, 1.0 \times 10^{-20}$	1.0×10^{-20}
Temperature, ℃	100	100

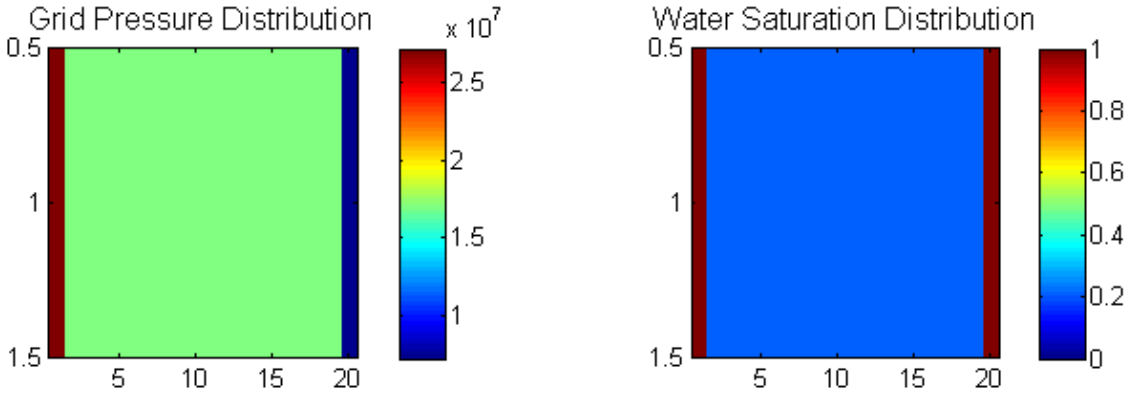

Figure 15: Initial condition of pressure and water saturation for 1D model.

2.4 2D Micro and Macro Models

After we described and explained the dynamic flow process of 1D model, the 2D micro and macro models are also built to show the water and gas phases flow in two dimensions. We will firstly introduced the 2D micro model and then 2D macro model, because the macro model has the same properties with the micro model except for larger grid scale.

The 2D **micro** model includes $12 \times 12 \times 1$ grids and the size of each grid for X, Y and Z are $1 \times 10^{-5}m, 1 \times 10^{-5}m, 1 \times 10^{-5}m$. The shale matrix contains 10×10 grids which are surrounded by natural fractures. To investigate the influence of kerogen matter on the two phases flow and nanoparticles transport, two different 2D micro and macro models are performed and compared as in Figure 16. One contains kerogen matter and the other does not include. In the Figure 16, the left matrix only contains the inorganic matter, where the blue color of inside grids represent the inorganic matter and the red color of outside surrounding grids stand for the fracture media. The right matrix of Figure 16 includes inorganic matter, organic matter, and fractures. The light green grids represent the organic matter, where 15% organic matter (15 grids) is randomly distributed among the shale matrix. One random function program is used to achieve the goal of random distribution of organic matter.

The main medium parameters for the 2D **micro** with and without organic matter are shown in Table 2. Same with 1D model, the fracture media has higher porosity and permeability, higher pressure, and higher nanoparticles concentration than the inorganic matter and organic matter. Since numerous adsorbed gas and free gas in kerogen matter

and desorption and adsorption physics play an important role on the gas production, diffusivity is considered in the organic matter for sure. Different with inorganic matter, the initial water saturation of organic matter is only 0.01 because organic matter is hydrocarbon-wet and no irreducible water saturation exists on the pore surface. Additionally, the models are also conducted under isothermal condition, so no heat transfer and loss need to be considered. Mass concentration of nanoparticles is used as indicator to show the change trend of nanoparticles, which is computed as Equation (18).

$$m_{NPs} = C_i \times \phi_i \times (S_w)_i \times Vol_i \quad (18)$$

Where m_{NPs} is the mass of nanoparticles, C_i is the concentration of nanoparticles, ϕ_i is the porosity of the grid, S_w is the water saturation, Vol_i is the volume of the grid.

In the 2D micro models, the water and nanoparticles could flow into all the matrix without any problem because of tiny scale. To investigate how far these nanoparticles could flow into the matrix on the same initial condition, the 2D macro models have been built. The mesh contains identical $12 \times 12 \times 1$ girds which include inorganic matter, organic matter, and fracture media. The grid size of X, Y and Z for the macro models are enlarged from $1 \times 10^{-5}\ m$ of micro size to $1 \times 10^{-1}\ m$ of macro size, and all the other reservoir properties and grids structure keep the same, just the same with the Table 2. With the large mesh size, to flow through one grid will take longer time and the total mass of nanoparticle in each grid will also increase because of larger volume. Two macro models with and without organic matter are presented and the change trend of water saturation and mass concentration of nanoparticles are also shown in a time sequence. As the same with the micro models, 15% organic matter (15 grids) is

randomly dispersed among the matrix on the macro matrix, and the mass concentration of nanoparticles is still used as indicator to display the change of nanoparticles.

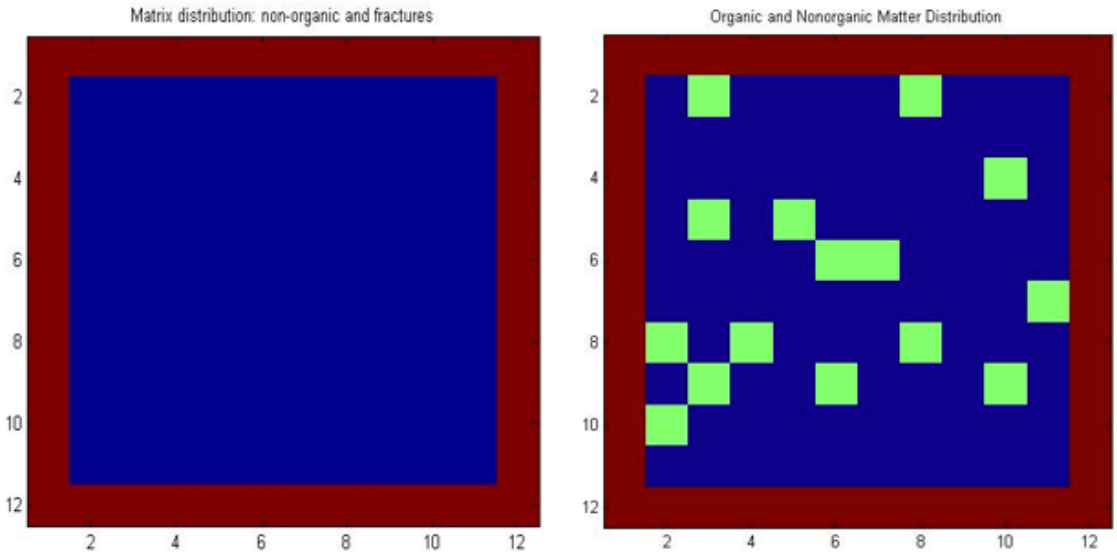

Figure 16: The distribution of nonorganic and organic matter in 2D micro matrix.

Table 2: Main parameters of the pore medium for the 2D micro and macro models

Pore Medium	**Fracture**	**Inorganic**	**Organic**
Density, $kg/m3$	--	2.6×10^3	1.35×10^3
Porosity	1.0	0.02	0.2
Permeability	84 mD	50 nD	50 nD
Diffusivity, m^2/s	--	--	8.21×10^{-5}
Pressure, Pa	2.72×10^7	1.72×10^7	1.72×10^7
Water Saturation	0.99	0.21	0.01
NPs Concentration, kg/L	1.0×10^{-6}	1.0×10^{-20}	1.0×10^{-20}
Temperature, ℃	100	100	100

2.5 Reservoir Model

So far, we have built up and shown the 1D micro model, 2D micro and macro models which could exactly display how does nanoparticles flow along with two phase in shale reservoirs and the changing trend of water saturation and concentration of nanoparticles. Since hydraulic fractures are one necessary and unavoidable part to make ultra-low permeability shale rock economically producible, so the dynamic processes looking at nanoparticles flowing from the wellbore to the fractures and then to the matrix are required to modeled to evaluate stimulation designs and nanoparticles injection plan. Taking into account that both the hydraulic fracture and complex fracture network need to be characterized in our reservoir model, a stimulated reservoir area (SRV) has been selected to represent the fractured shale reservoir in our model as Figure. 17. The SRV contains four various pore systems, where blue grids stand for well bore, red grids represent hydraulic fractures, light green stand for natural fractures, and the rest of white girds are shale matrix. Based on the conclusion obtained from the 2D models that nanoparticles and water are quite limited to flow into the organic matter, the matrix only contains non-organic matter in this large reservoir model. Each of various grid has different size in x and y axis, while they have same size in z axis, $0.01\ m$. The sizes of matrix grids on x and y axes are $1.0\ and\ 1.0\ meter$, and the size of natural fracture grids on x and y axes are $0.01\ and\ 0.01/1.0\ meter$, and the size of hydraulic fracture girds on x and y axes are $0.05\ and\ 1.0/0.01\ meter$, and the size of wellbore grids on x and y axes are $1.0/0.01\ and\ 1.0\ meter$.

In our model, gas and water are only flowing into the wellbore through the hydraulic fractures and no directly connections between shale matrixes and wellbore exist. Shale matrix (non-organic matter grid) has directly connection with natural fractures and hydraulic fractures, but water and gas have to flow into the natural fractures and then into the hydraulic fractures in most non-organic grids. Moreover, the well bore acting as the supplier of nanoparticles have higher water saturation and higher concentration of nanoparticles, while the shale matrix and natural fractures hold higher pressure than the hydraulic fractures and wellbore. Table 3 shows the main initial parameters for the stimulated reservoir volume and wellbore used for the simulator. The porosity of inorganic matter is only 0.02 and the all others medium have the porosity 1.0. From the wellbore to hydraulic fracture to natural fracture to inorganic matter, the permeability decreases. The water saturation of natural fracture is 0.4 which means lots of gas exists. The water saturation of inorganic matter is 0.21, which is almost equal to its irreducible water saturation. Same with previous numerical models, this large reservoir model is also performed in isothermal condition, so we don't need worry about the heat and energy loss and transfer.

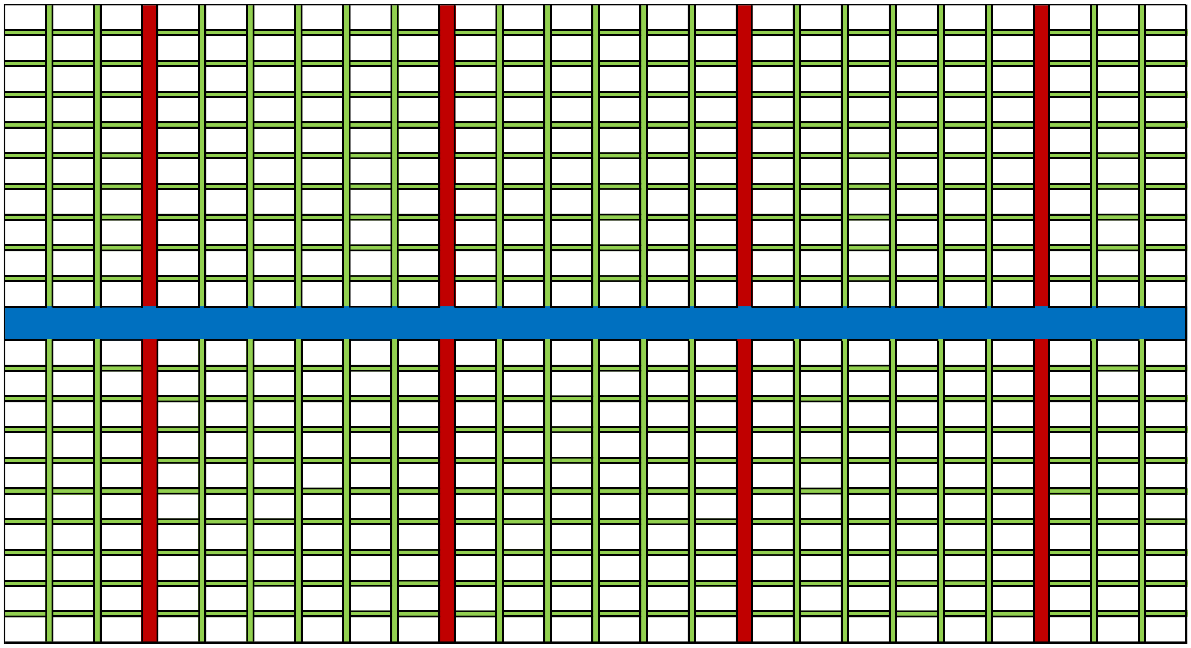

Figure 17: A sketch of multiple hydraulic fractured horizontal shale gas well.

Table 3: Initial parameters of stimulated reservoir volume and Wellbore

Initial Parameters of Stimulated Reservoir Volume					
Porosity Media		Inorganic	NF	HF	Wellbore
Size (m)		$1 \times 1 \times 0.1$	$1 \times 0.01 \times 0.1$	$1 \times 0.05 \times 0.1$	$1 \times 1 \times 0.1$
Porosity		0.02	1.0	1.0	1.0
Permeability		50 nD	84 mD	420 mD	8.4 D
Pressure (MPa)		27.2	27.2	4.0	4.0
Sw		0.21	0.4	0.99	0.99
Concentration (Kg/L)		1×10^{-20}	1×10^{-20}	1×10^{-20}	1×10^{-6}
Temperature (F)		100	100	100	100
Size (m)	X	1.0	0.01	0.05	1/0.01
	Y	1.0	1/0.01	1/0.01	1.0
	Z	0.1	0.1	0.1	0.1

2.6 Magnetism Analysis

In this project, synthesized Magnetic Carbon-Coated Iron-Oxide Nanoparticles is applied as the model nanoparticle example. These super-paramagnetic iron oxide nanoparticles are synthesized by the solvothermal chemical method (Lu et al. 2007). Nuclear magnetic resonance (NMR) refers to the response of magnetic dipoles of hydrogen nuclei in the presence of an applied magnetics field. The NMR technique can capture the magnetic signal which is released by hydrogen nuclei when they are return to their original state after an external magnetic field changed the position of atomic nucleus. As the equation (19) shows, Magnetic susceptibility is the degree to which a material can be magnetized in an external magnetic field. Since H is the applied external field, the magnetization of material is up to how strong the volume magnetic susceptibility is.

$$M = x_m \times H \tag{19}$$

$$M_{total} = (x_{m_{water}} + x_{m_{methane}} + x_{m_{nano}}) \times H \tag{20}$$

Where M is magnetization of the material, x_m is volume magnetic susceptibility, H is magnetic field strength, the applied external field. Therefore, the total magnetization at the shale reservoir is mainly made up of water, methane and nanoparticles as the equation (20).

Fortunately, the magnetic susceptibility of water and methane can be obtained from references (Arrighini et al. 1968). In our model, the value of magnetic susceptibility of water we used is 9.035×10^{-6} at 20℃, and the value of magnetic

susceptibility of methane is 9.13×10^{-9} at 20℃. The magnetic susceptibility of magnetic nanoparticles could be calculated by using the equation (22) and (23). Equation (21) is regarded as Curie's law, where susceptibility x_m of paramagnetic materials is inversely proportional to their temperature. However, our reservoir models are performed in isothermal status, so we don't consider the change of temperature. For a paramagnetic ion with non-interacting magnetic moments with angular momentum J, the Curie constant is related the individual ion's magnetic moments in equation (22). Therefore, based on the previous results of the distribution of water saturation and nanoparticles concentration, the volume magnetic susceptibility could be easily computed through these equations.

$$x_m = C/T \tag{21}$$

$$C = \frac{N_A}{3k_B}{\mu_{eff}}^2 = \frac{N_A}{3k_B}{\mu_B}^2 \left(\frac{\mu_{eff}}{\mu_B}\right)^2 \tag{22}$$

$$C_{vol} = C \times \Phi \times S_i \times V_{grid} \tag{23}$$

Where C is a material-specific Curie constant, T is absolute temperature in kelvins, N_A is number of magnetic atoms per unit volume, k_B is Boltzmann's constant: $1.3806488 \times 10^{-23}\ J/K$, μ_{eff} is the effective magnetic moment per paramagnetic ion, μ_B is the Bohr magneton: $9.27400968 \times 10^{-24}\ J/T$, C_{vol} is volume magnetic susceptibility, ϕ is porosity of each grid, S_i is saturation of water or gas in grid, V_{grid} is the grid volume (BBI Solution, 2014; Wikipedia, 2014; SPE PetroWiki, 2014; The Engineering ToolBox, 2004).

Table 4: The value of Bohr magneton and effective magnetic moment

The value of Bohr magneton

system of units	value	unit
SI[1]	$9.27400968(20) \times 10^{-24}$	$J \cdot T^{-1}$
CGS[2]	$9.27400968(20) \times 10^{-21}$	$Erg \cdot G^{-1}$
eV[3]	$5.7883818066(38) \times 10^{-5}$	$eV \cdot T^{-1}$
atomic units	$1/2$	none

μ_{eff} values for typical d^3 and d^5 transition metal complexes.[5]

Material	μ_{eff}/μ_B
$[Cr(NH_3)_6]Br_3$	3.77
$K_3[Cr(CN)_6]$	3.87
$K_3[MoCl_6]$	3.79
$K_4[V(CN)_6]$	3.78
$[Mn(NH_3)_6]Cl_2$	5.92
$(NH_4)_2[Mn(SO_4)_2] \cdot 6H_2O$	5.92
$NH_4[Fe(SO_4)_2] \cdot 12H_2O$	5.89

Overall, based on these equations above and the results about the distribution of water saturation and nanoparticles concentration from the previous models, the volume magnetic susceptibility and total magnetization of reservoir could be computed and presented. Two different reservoir modes with and without the magnetic nanoparticles are conducted to investigate the influence of these magnetic nanoparticles on the results of magnetism analysis. Moreover, the results we obtained from our numerical reservoir models will be compared with some experimental data to validate the availability and effectiveness of this simulator.

CHAPTER III

RESULTS ANALYSIS

3.1 Results for 1D Model

Based on the pressure difference, the major flow direction will be from left side to right side on the Figure 15. The distribution of pressure and concentration is presented from early time to final time on Figure 18. The left graph is for the distribution of grid pressure, where the numbers on x axis represents the grid numbers, from grid 1 to grid 20, and the y axis only has one grid, and the pressure range is from $1.72 \times 10^7 \; to \; 3.20 \times 10^7 \; pa$. The right graph is for the distribution of water saturation, and the value is from 0 to 1. Due to the pressure difference, water is imbibed into the middle grids to increase their water saturation and pressure. Because the middle grids' pressure is smaller than the fracture gird, so the gas cannot flow out and is compressed in the grid. More and more water and nanoparticles flow into the middle grid, and their pressure keep gradually increasing. One special point is the middle gird pressure reaches equal to the fracture pressure. However, due to water is wetting phase in non-organic matter and its mobile water pressure is lower than its grid pressure, so the water continues to invade from the fracture gird into the middle grids until both water mobile pressure achieves equal. Besides, gas phase starts to flow from the non-organic gird out to the fracture grid on this special point. Because the last right matrix grid pressure is larger than the right fracture grid pressure, so the gas will flow out into the fracture and its pressure will drop. When the last right matrix grid pressure decreases to equal with the fracture grid, the gas

stops flowing out. Since that point, at the same time, water will flow from the right fracture grid into the last right matrix grid because of the pressure difference of water mobile phase. So you could find last right matrix grid have higher water saturation than the middle matrix grid.

The normal pressure gradient should decrease from left to right, while the capillary pressure effect leads to the difference that some non-organic girds pressure became higher than the fracture pressure, in order to they have the same mobile pressure of water phase. The gap between the first non-organic grid and the fracture gird is nearly equal to the capillary pressure, which proves the theory mentioned above. Moreover, this pressure gap almost keep the same when we changed the pressure distribution among the fractures and non-organic grids, for example, we increase the pressure of left fracture grid, because the capillary pressure is related to water saturation and rock properties, not the given pressure value. A obvious concentration gradient can be found in Figure 18, which shows nanoparticles is typically flowing from the injection grid (the fracture gird) into the matrix, and the concentration of nanoparticles will keep dropping when it goes far away from the nanoparticles source.

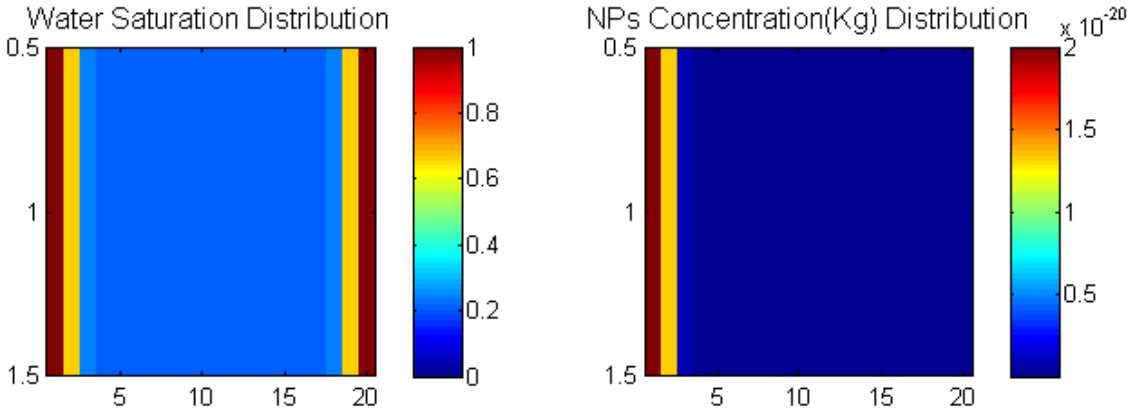

(a) Early time

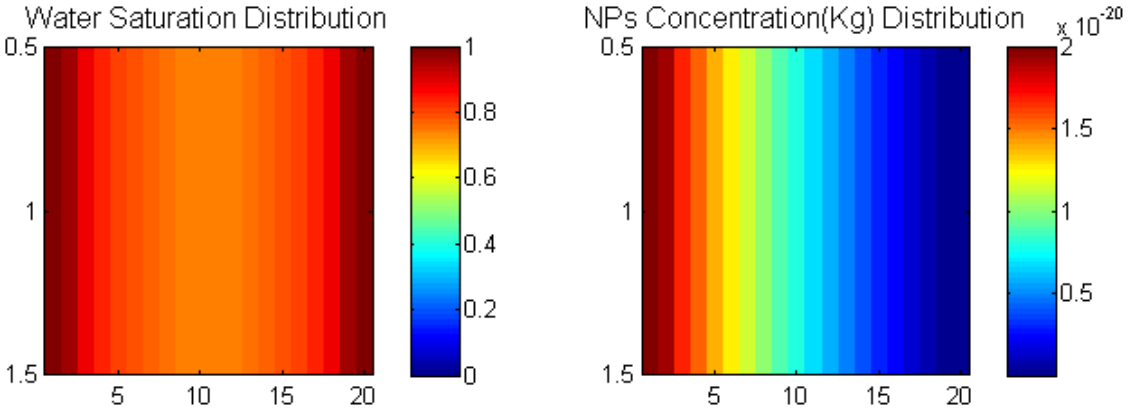

(b) Middle time

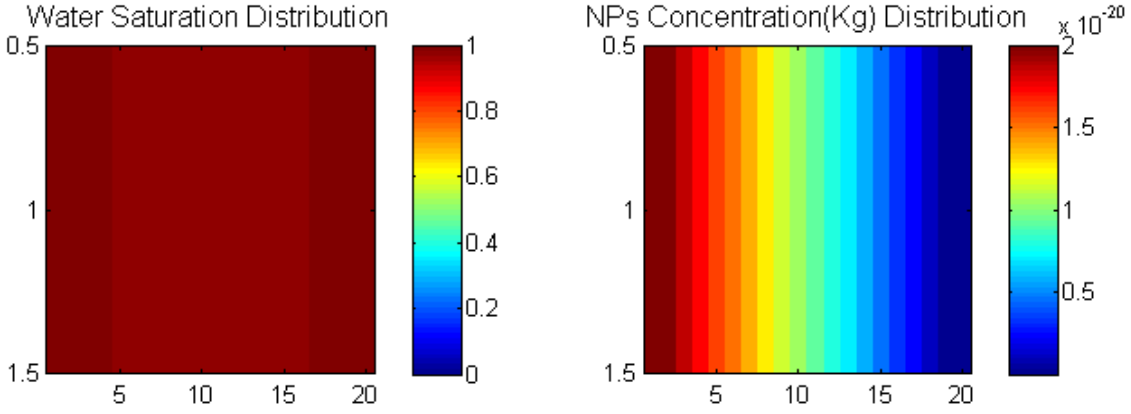

(c) Final time

Figure 18: The distribution of water saturation and nanoparticles concentration at different time steps in the 1D model.

3.2 Results for 2D Micro Models

In 2D micro models, water is flowing from the surrounding fractures into the matrix and gas is drained out, because the fracture grids hold the higher pressure and water saturation than the matrix. On the Figure 19 and 20, the changing trend of water saturation and mass concentration of nanoparticles is displayed in a time sequence. In the micro model with only non-organic matter, nanoparticles are flowing into the shale matrix along with water phase and obviously they have similar varying pattern, as from the early time stage to final time stage on the Figure 19. The numbers of X and Y axes on the figures represent the grid number, from first grid to 12^{th} grid. The value range for water saturation is from zero to one, and the value range for nanoparticles concentration is from $3.3 \times 10^{-31}\ to\ 2.0 \times 10^{-20}\ kg$. Actually most nanoparticles entered the matrix at only about 2.4 second because of micro size scale, while it achieves a steady status at 1.29×10^{2} second. The pressure finally reaches equal between the fracture grids and middle grids. Also the water saturation and nanoparticles concentration reach equal at the final time stages, which means the water and nanoparticles enter all the matrix.

However, the dynamic flow in the micro model with organic matter is different with that of only non-organic model even though at the same initial condition. 15% organic matter is randomly distributed among the matrix, some of which are connected with the surrounding fractures and others are only connected with the non-organic grids, as on the right graph of Figure 20. Different with the non-organic matter, gas is wetting phase in the organic matter, so no capillary pressure difference exists for the water phase in organic grids. The mobile water pressure of organic grids is increasing along with the

invasion of water from the fractures and it is eventually equivalent with the fractures pressure which means no more water flow in. Besides, high capillary pressure prevents gas phase outflow at the same time in organic grids. Conversely, more water could flow into the non-organic grids because mobile water pressure is reduced by high capillary pressure in non-organic grids. In other words, the mobile water pressure is not equal between non-organic and organic grids even though the grid pressure finally arrive equal with the fracture grids. As from the early time to final time on the Figure 20, water and nanoparticles are gradually flowing into the matrix. Compared with the previous non-organic model, the non-organic grids have the same flow phenomenon, while apparently water phase experience some difficulty to flow into the organic girds. In addition, when connected with the fracture grids with high permeability, the organic girds could reach at a higher water saturation and mass of nanoparticles than these grids only connected with non-organic grids. Due to the porosity of organic vugs (0.2) is 10 times larger than that of the non-organic grids, the mass of nanoparticles in these organic grids which share the high fracture permeability by directly connecting with the fracture grids, is bigger than that of non-organic grids although the organic grids contain smaller water saturation. However, as on the part (c) of Figure 20, most organic girds only get litter improvement on water saturation and mass of nanoparticles such as from 0.01 to 0.02.

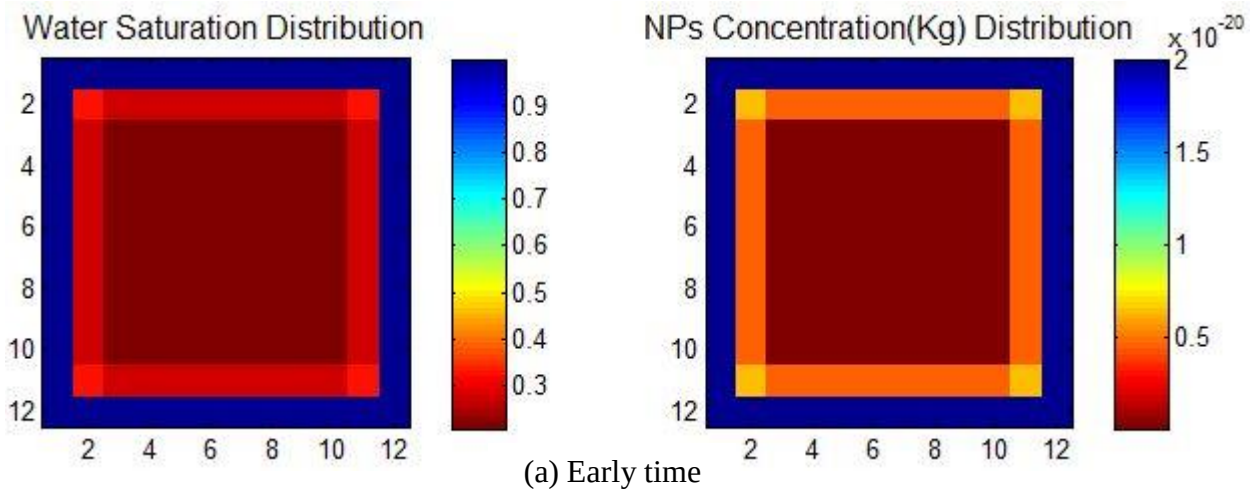

(a) Early time

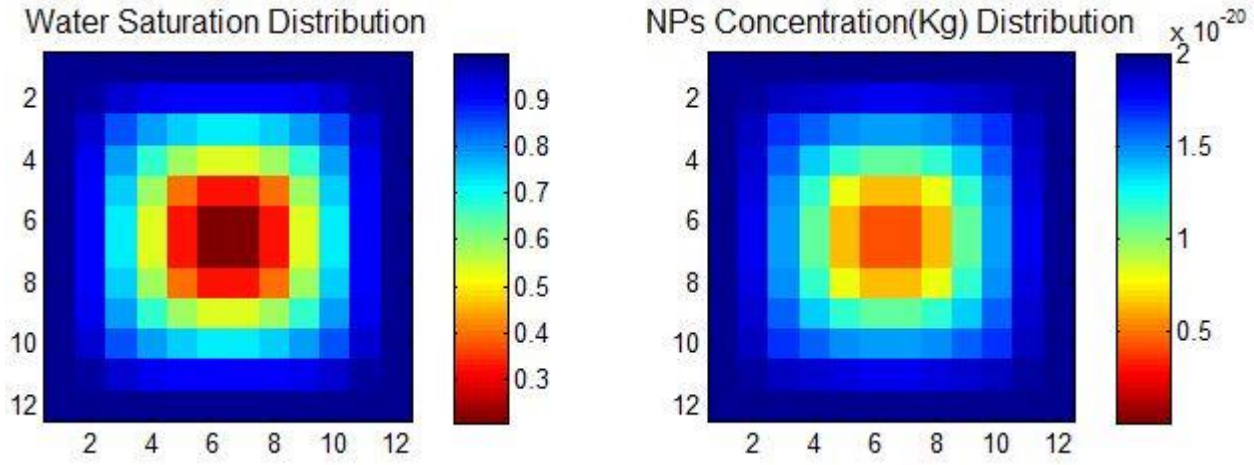

(b) Middle time

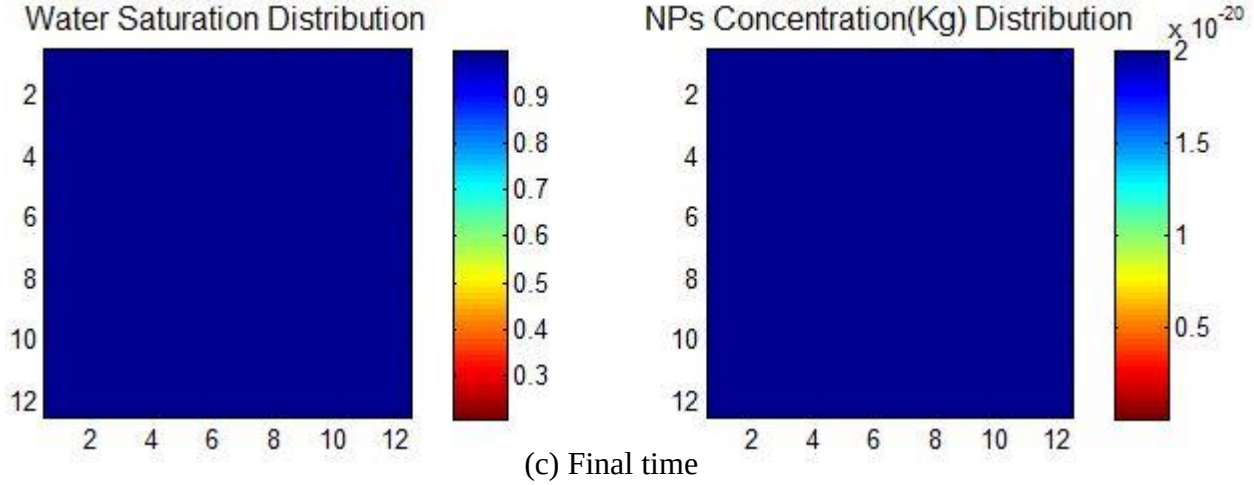

(c) Final time

Figure 19: The distribution of water saturation and nanoparticles concentration at different time steps in the 2D micro model without organic matter.

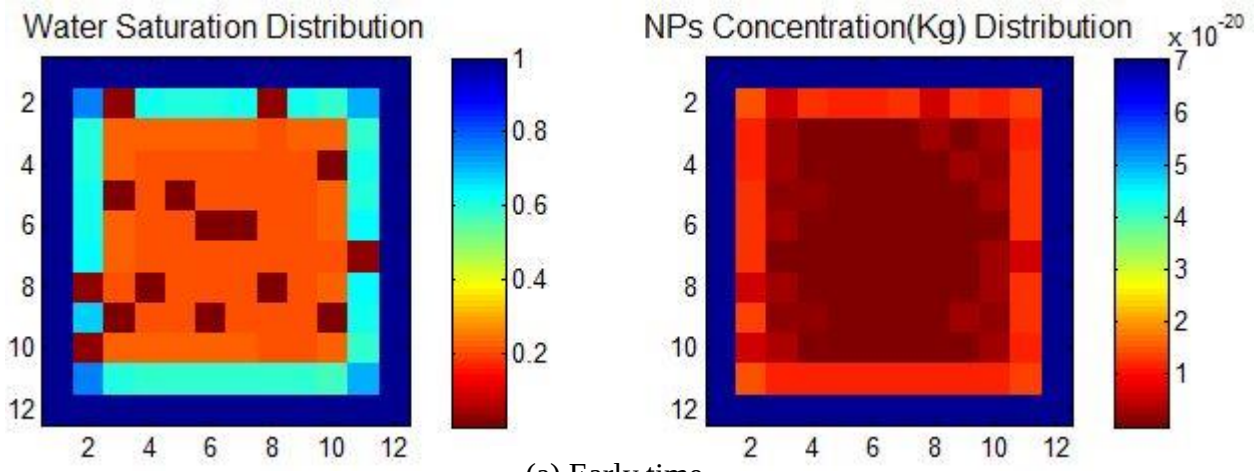

(a) Early time

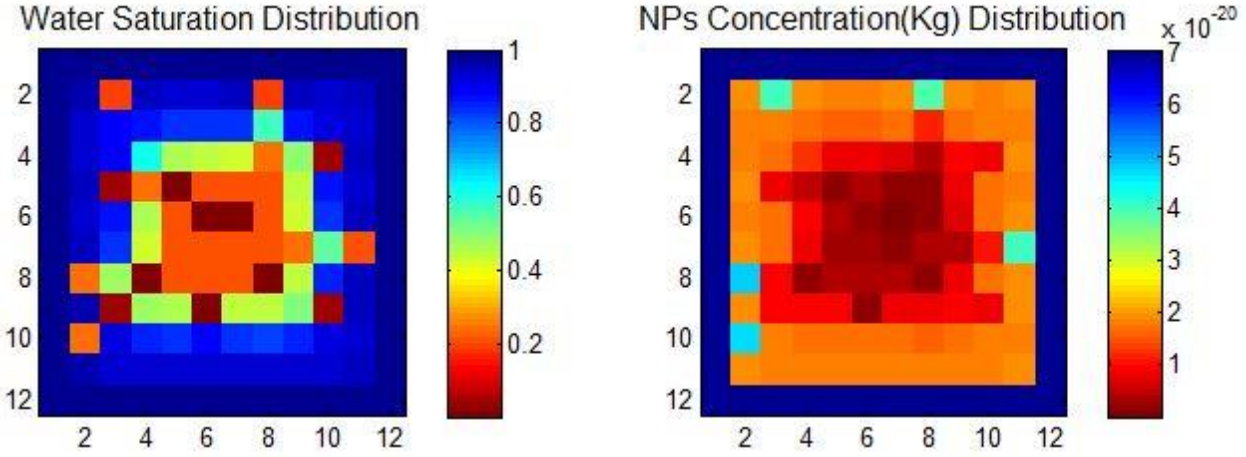

(b) Middle time

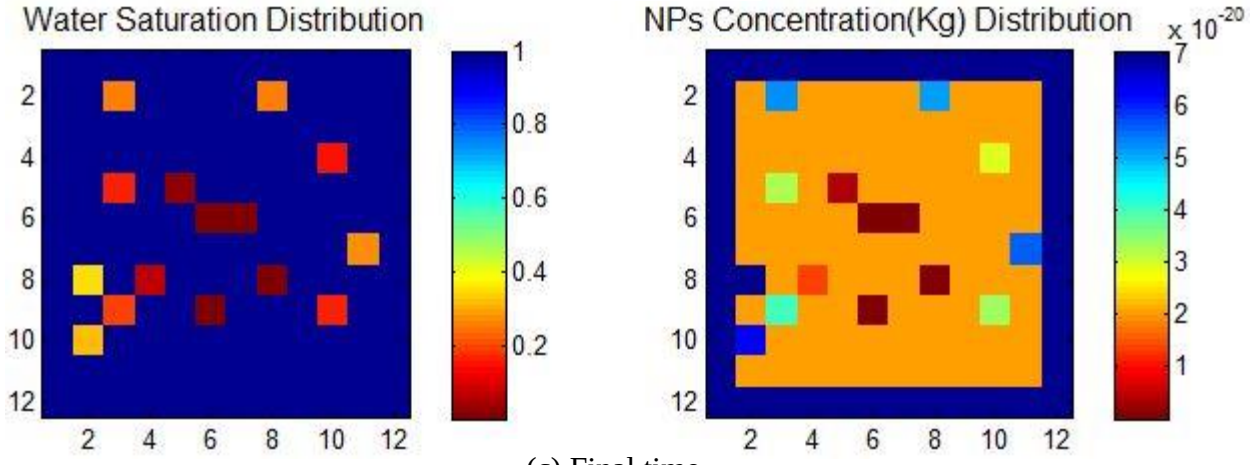

(c) Final time

Figure 20: The distribution of water saturation and nanoparticles concentration at different time steps in the 2D micro model with organic matter.

In addition, the plots about total nanoparticles mass along with time are shown for the micro modes without organic matter on Figure 21. After the nanoparticles mass in each grid was calculated by using Equation (18), we sum up all the matrix grids to get the total mass of nanoparticles in matrix. As you could see, the total mass of nanoparticles goes up along with time and reach stable status at the last stage. In other words, the nanoparticles are gradually flow into the matrix until it cannot enter the matrix any more. This plot could mainly tell two key information: one is how much nanoparticles in total could flow into the matrix, other one is how long the process takes. The plot shows all the nanoparticles enter the matrix in a very short time for the micro model while it needs much longer to reach convergent status. Because of tiny grid scale, this micro model took about one second to reach stable status, while it took about two minutes for the simulator achieving convergent status.

Moreover, to verify and confirm the numerical results, we refine the shale mesh into two times and four times, where two times refine means one grid is refined into four equal smaller grids, two in one dimension. With the same initial reservoir condition, we performed the 2D micro model on different mesh grids. As usually, the smaller girds or more fine mesh could provide more accurate results. As shown on Figure 21, we plot the results from different mesh and compare them with each other. The blue curve is for the mesh without any refine, and the red curve is for the two times refined mesh, and the green yellow is for the four times refined mesh where one grid is refined into 16 equal smaller grids, four in one dimension. The basic matrix without refine and the refined matrixes have the almost the same results about total mass of nanoparticles, and also

provide same curves for the variation of the total nanoparticles mass along the time. Therefore, the results we obtained is correct. Of course, the refine mesh always need more computation ability and takes longer time to perform.

Brownian diffusion and convection flow are two flow mechanisms for the transport of nanoparticles. To investigate the effect of nanoparticles diffusion and how much it contributes to the total movement, we performed two micro models including organic matter with and without Nanoparticle diffusion and compare their results. As the Figure 22, the blue curve presents the model where diffusion of nanoparticles is considered and the red curve did not take into account the diffusions mechanism. Clearly the blue curve has larger total mass of nanoparticles than the red curve because it has two flow contributions. In the both models, the total mass of nanoparticles are rapidly increasing along the time and reach stable status at the later stage. After comparing this two models and computing in the equation (24) below, we found the Brownian diffusion contributes about 18% of the transport of nanoparticles. In other words, the convection flow is the major flow mechanism for nanoparticles.

$$\frac{With\_Diff - Without\_Diff}{With\_Diff} = \frac{2.148\times10^{-8} - 1.766\times10^{-8}}{2.148\times10^{-8}} = 18\% \quad (24)$$

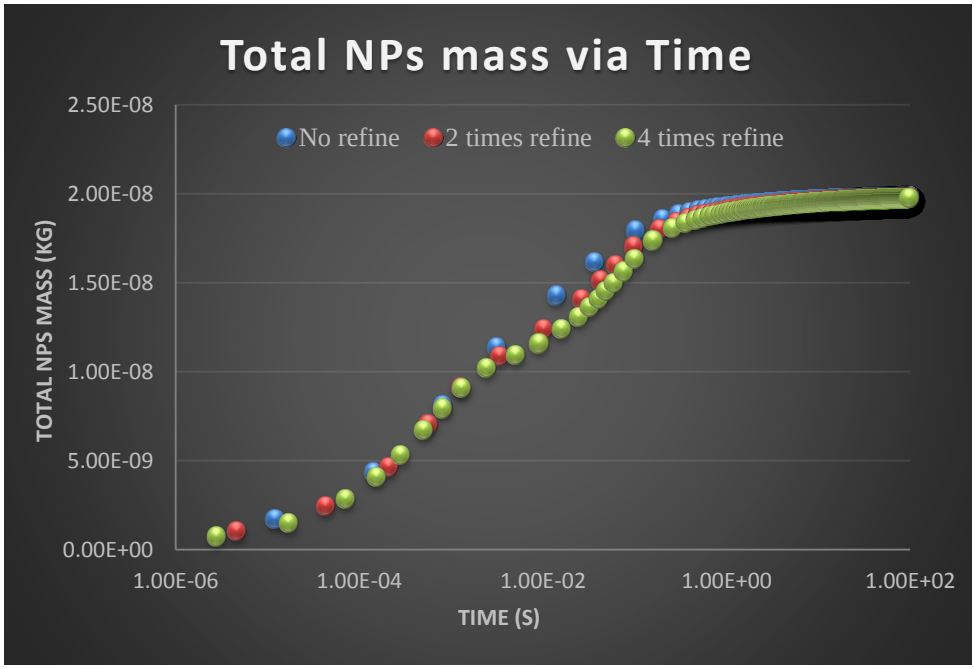

Figure 21: Total nanoparticles mass along with time in the micro models without organic matter.

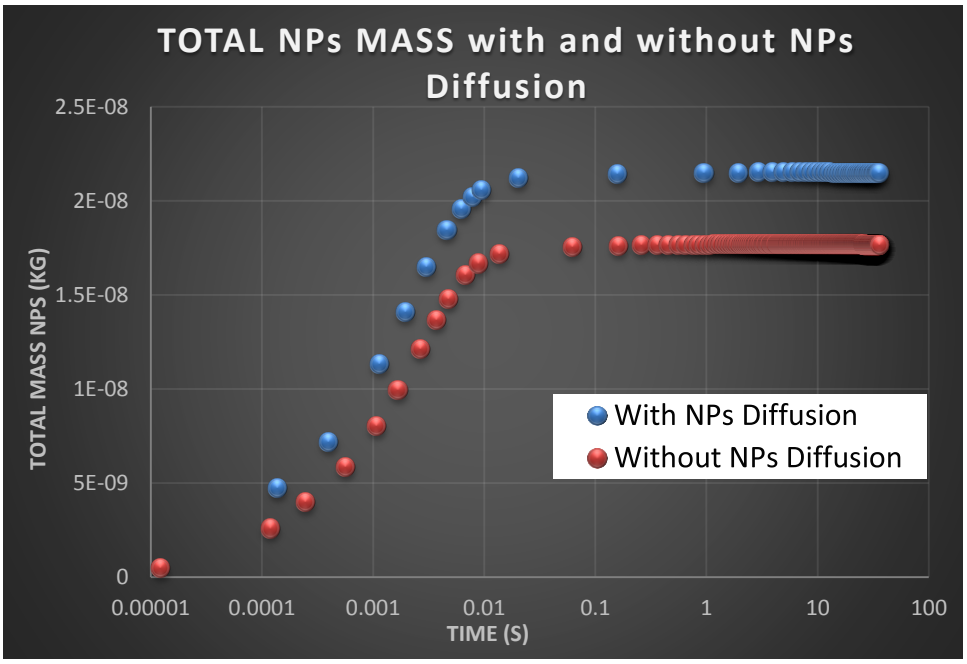

Figure 22: Total mass of nanoparticles for 2D micro models including organic matter with and without nanoparticles diffusion.

Overall, based on the results from the micro model with and without organic matter, we could found that water and nanoparticles can quickly flow into the non-organic grids for the micro models, while it is limited to flow into the organic matter if they are not connected with the fracture grids. In other words, it is very limited and difficult to flow from the non-organic matter or organic matter into the organic matter. The major invasion of water phase and nanoparticles could be completed in an extremely short time. Moreover, the Brownian diffusion mechanism contributes about 18% to the entire transport of nanoparticle movement.

3.3 Results for 2D Macro Models

In the 2D micro models, the water and nanoparticles could flow into all the matrix because of tiny scale size. The 2D **macro** models are introduced as following to present how far these nanoparticles can really flow into the shale matrix with the same initial reservoir condition. The grid size of x, y and z are enlarged from $1 \times 10^{-5}\ m$ of micro size to $1 \times 10^{-1}\ m$ of macro size, while all the other reservoir properties and grids structure keep the same, just the same with the Table 2. Also to investigate the influence of organic matter, two macro models with and without organic matter are displayed and the distribution trend of water saturation and mass concentration of nanoparticles are also shown in a time sequence. As the same with micro models, 15% organic matter (15 grids) is randomly dispersed among the matrix on the macro model, and the mass

concentration of nanoparticles is still used as indicator to display the changes of nanoparticles.

In the 2D macro model without organic matter, the water is flowing into the matrix and gas is drained out due to the pressure and concentration difference between surrounding fractures and middle matrix. As from the early time to final time on the Figure 23, water phase and nanoparticles are gradually flow into the matrix and they have the similar change trend. However, the nanoparticles could only invade two grid blocks, about 20 centimeters, before the simulator reaches convergence. In other words, the nanoparticles cannot flow into the matrix any further. If we do not consider the outside surrounding fracture grids, the water saturation of first outside surround matrix grids reach about 0.84 while its pressure is even bigger than the fractures pressure. The pressure in this thesis means wetting phase pressure of the grid. Because water is wetting phase in non-organic matter, and there is a big capillary pressure effect on water movement. The fracture grids and first outside surrounding matrix grids could still have equal water pressure, even though the matrix girds have higher pressure. Therefore, they could reach the stable status. The water saturation of second surrounding grids arrive at about 0.38 and water saturation of the rest of matrix grids increased a little bit. The distribution of nanoparticles is similar with water saturation. As the Figure 23, the nanoparticles could also only flow about 2 grids distance into the matrix. The second surrounding grids did not even reach the high nanoparticle concentration, and the third surrounding grids did increase a litter on the concentration of nanoparticles.

Looking into the 2D macro model with organic matter on Figure 24, the changing trend of water saturation and nanoparticles is quite similar with the micro models. From the early time to final time on Figure 24, water and nanoparticles are easy to flow into the non-organic grids while experiencing difficulty to enter these organic grids except for the grids directly connected with the fractures. For these grid connected to the fractures, the reason they have large mass concentration of nanoparticles is they have bigger porosity as mentioned above.

The most important information we could obtain from macro models is that water phase and nanoparticles could only flow into shale matrix with limited distance. Besides, compared to the long time to reach the final stable status, the majority invasion of water and nanoparticles could be completed in a short time.

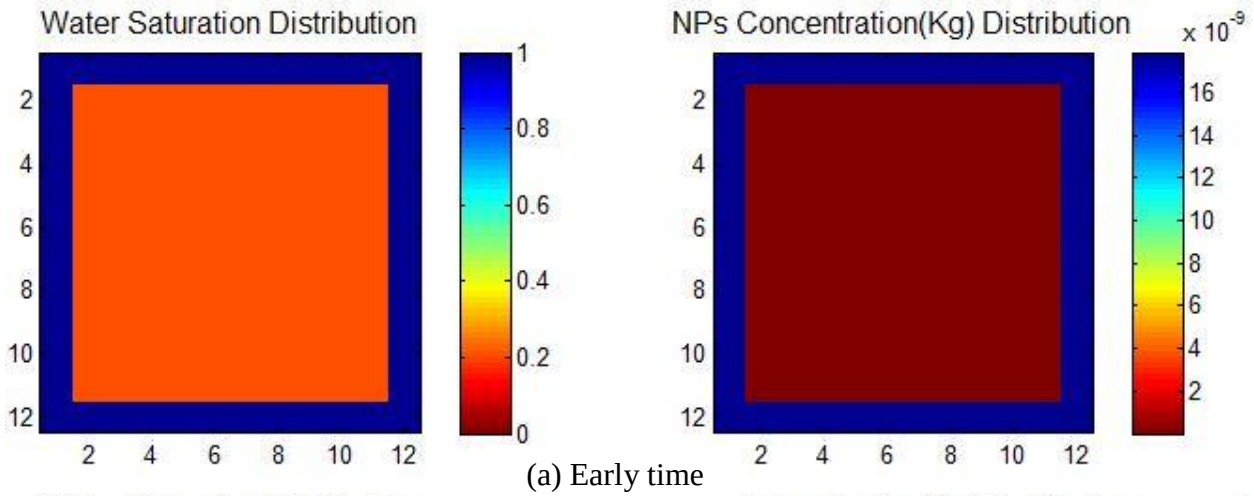

(a) Early time

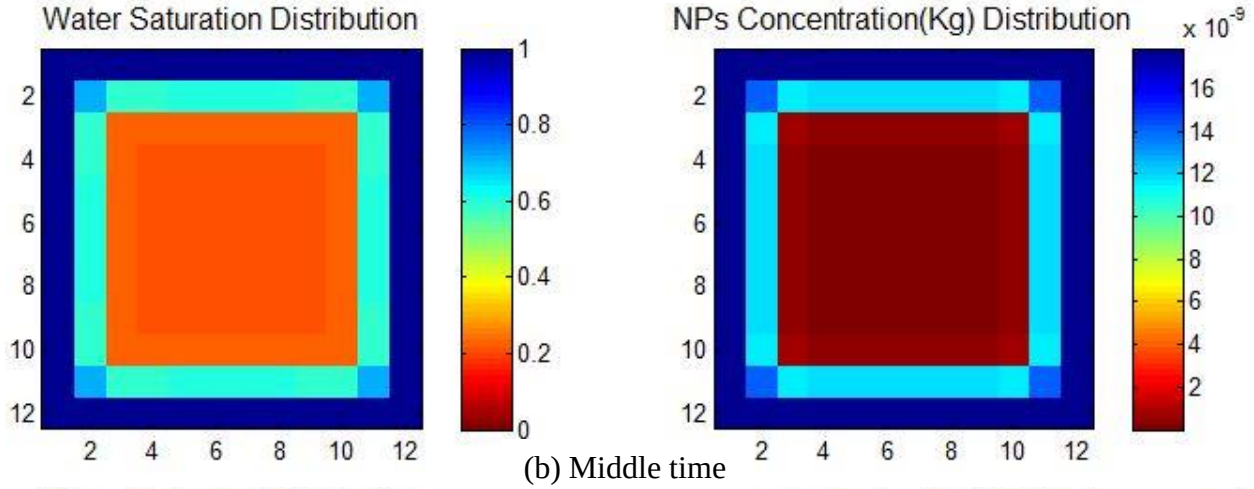

(b) Middle time

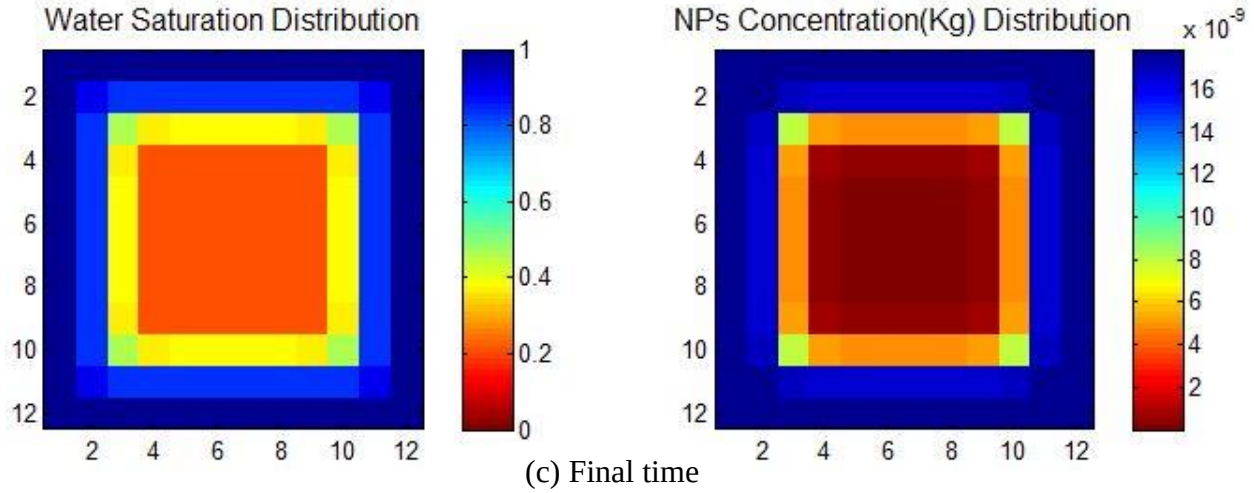

(c) Final time

Figure 23: The distribution of water saturation and nanoparticles concentration at different time steps in the 2D MACRO model without organic matter.

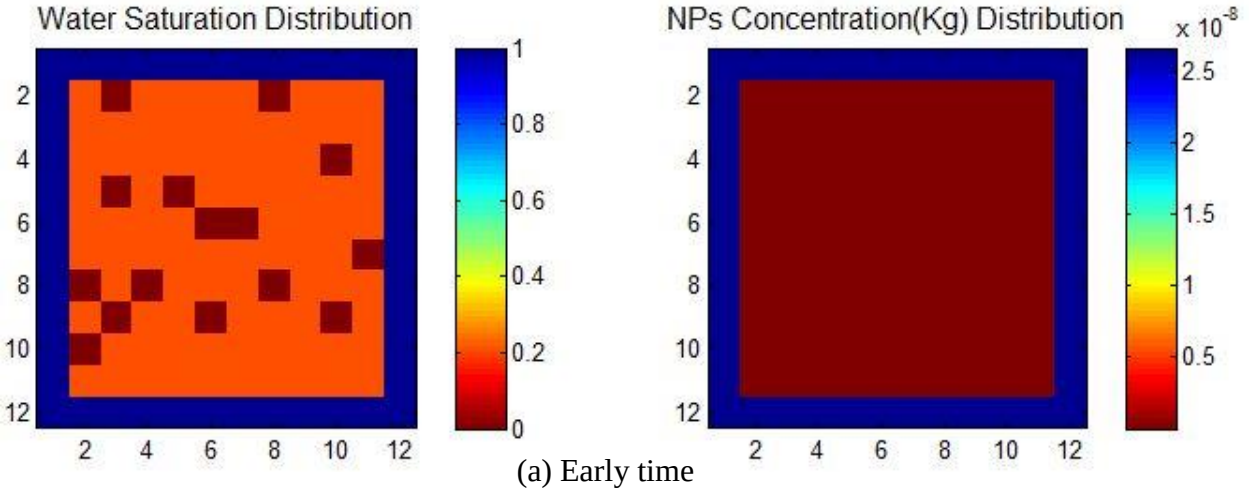

(a) Early time

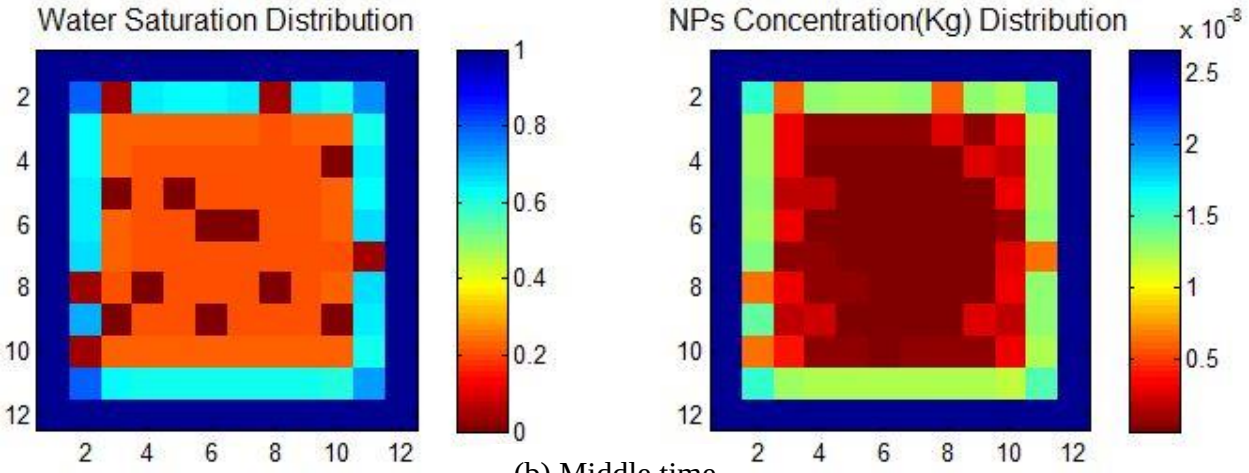

(b) Middle time

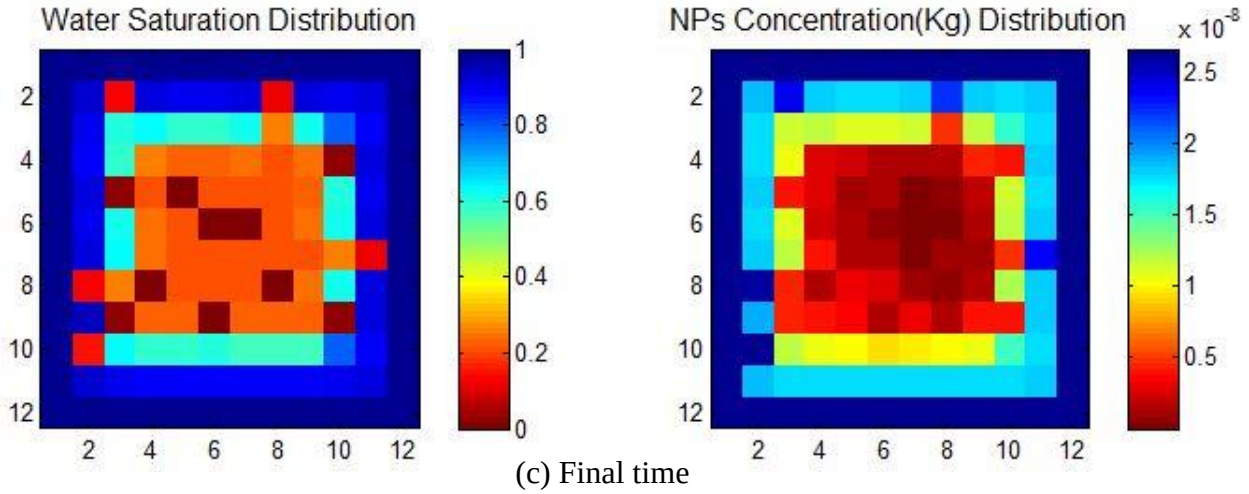

(c) Final time

Figure 24: The distribution of water saturation and nanoparticles concentration at different time steps in the 2D MACRO model with organic matter.

3.4 Results for Large Reservoir Model

As the Table 3 and Figure 17 show, the shale matrix includes the inorganic matter and natural fractures, hydraulic fractures, and wellbore system. Figure 25 shows the distribution of pressure and water saturation at the initial condition. On the left graph, the horizontal red grids represent wellbore, and the four vertical grids stand for hydraulic fractures, and the rest of grids are shale matrix including inorganic matter and natural fractures. The numbers on the x and y axes are the grid numbers: x axis is from grid one to grid forty seven, and y axis is from grid one to grid thirty nine. The pressure range for the initial reservoir is from $4.0 \times 10^6\ to\ 2.72 \times 10^7\ Pa$. The right graph of Figure 25 is the water saturation distribution for the entire reservoir, where you could see the inorganic matter is just like small islands separately isolated among the natural and hydraulic fractures because this is stimulated reservoir volume. The matrix including inorganic matter and natural fractures has a higher initial pressure than the hydraulic fractures and well bore, which will result in gas flowing out from the shale matrix into the hydraulic fractures. Meanwhile, water is acting as wetting phase in the inorganic matter, which leads to a lower flowing pressure of water phase in inorganic matter because of high capillary pressures. The Figure 11 indicates a capillary pressure curve at various water saturation, where the capillary pressure is very high when the water saturation is only 0.21.

What should be pointed out on Figure 17 is that one pore system has connections with more than one another pore systems, which will be explained as below. Most inorganic matter are only connected with natural fracture grids, while some are also

connected with hydraulic fracture grids at the same time. For the natural fracture grids, they have connection with inorganic matter, natural fractures, and hydraulic fractures. Based on the difference of permeability, grid pressure, and other properties of these pore systems, these different connections would bring various flow results. On the Figure 26 below, the distribution of water saturation and nanoparticles mass are displayed at three different time steps: early, middle and final stages, where the exact time is also shown.

For the inorganic matter, gas is flowing out from the inorganic matter into the hydraulic fractures, and water is flowing from the hydraulic fractures and natural fractures into the inorganic matter. Due to water is wetting phase and a high capillary pressure exists for water phase in inorganic matter, so the natural fracture girds have a higher mobile water pressure than the inorganic grids. As a consequence, the pressure of inorganic matter decreases and its water saturation goes up.

For the natural fracture grids **without** connection with hydraulic fractures, water is flowing out from the natural fracture grids into the inorganic grid while gas is flowing form the inorganic matter into the natural fracture grids. For the natural fracture grids **with** connection with hydraulic fractures, water is flowing out from the natural fracture grids into the hydraulic fractures because of high pressure gradient. As a results, the grid pressure rises and the water saturation decline for all the natural fracture grids.

For the hydraulic fracture grids, there are two different type of reaction and change of pressure and water saturation. For the hydraulic fracture grids connected with inorganic matter, numerous gas is flowing from the inorganic grids into the hydraulic fracture grids and water is flowing in the inverse direction, which results in that the grid

pressure keeps going up and water saturation keeps dropping in these hydraulic fracture grids. However, for these hydraulic fracture grids only connected with natural fractures, both of gas and water are flowing from the natural fracture grids into the hydraulic fractures, because capillary pressure effect is not considered in the natural fracture grids. So the grid pressure and water saturation of these hydraulic fractures keep increasing.

Figure 26 (a) displays the distribution results about water saturation and nanoparticles concentration after 50.2 seconds. Due to wellbore acts as nanoparticles source, the water and nanoparticles start to flow from the hydraulic fractures into the inorganic matter grids. Because of pressure difference, gas would flow out from the hydraulic fractures into the wellbore and be produced, and the water phase including magnetic nanoparticles are gradually imbibed into the hydraulic fracture grids. You could clearly see the exact same invasion phenomenon in the right graph of Figure 26 (a).

Figure 26 (b) shows the dynamic process after the early stage, where more gas will flow out from the inorganic matter into the hydraulic fractures and well bore, and more and more nanoparticles and water are imbibed into the hydraulic fractures. Moreover, the nanoparticles could also flow into the inorganic matter and natural fracture girds along the water phase further and further.

Figure 26 (c) presents the final time step of the simulation after 2.5×10^9 second. The nanoparticles spread into everywhere of the matrix and reach to a high level value. The pressure at the hydraulic fractures everywhere is about the same while the water saturation varies depending on its location. The grids directly connected with the

natural fractures keep a high value of water saturation, while the grids connected with the inorganic matter have a low value, which confirms what is discussed above. On the right graph of Figure 26 (c), the reason why the mass of nanoparticles is not equal everywhere is that the grid volume is different even though the nanoparticles concentration is very close. As the Table 2, the inorganic grids is much larger than the hydraulic fracture grids, and the hydraulic fracture girds is five times bigger than the natural fracture girds. Consequently, the total mass are dissimilar after multiplying the different grid volume. In additional, the nanoparticles mass of well bore is assumed to biggest and constant, so their value and color are never changed in the Figure 26.

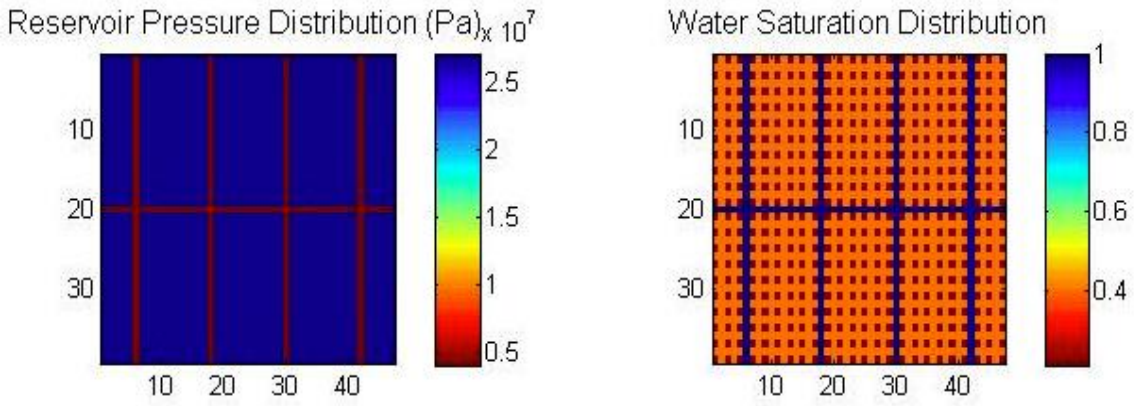

Figure 25: The distribution of grid pressure and water saturation at the initial condition.

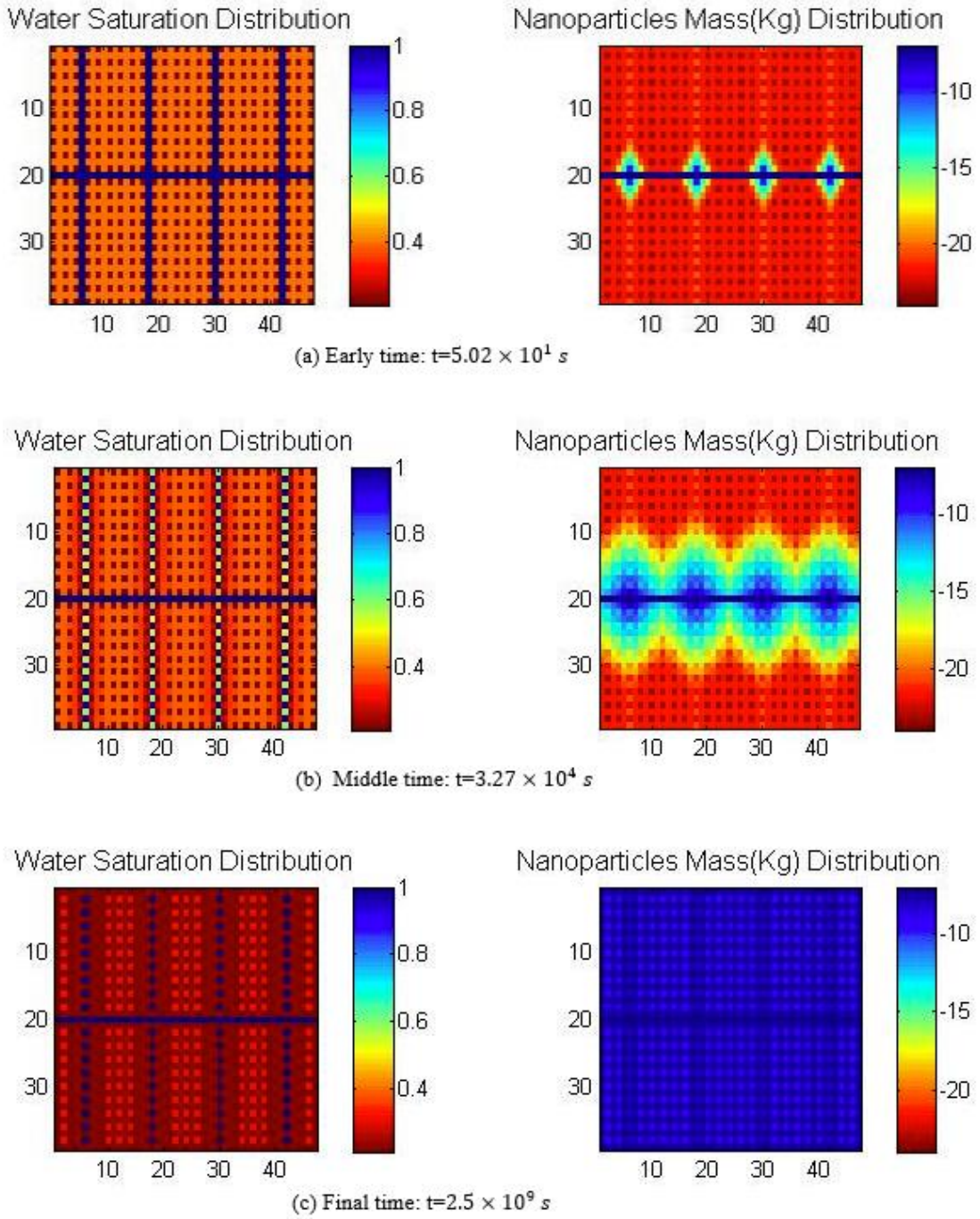

Figure 26: The distribution of water saturation and nanoparticles concentration at different time steps in the Reservoir Model.

As the same with previous 2D models, the total mass of nanoparticles representing all the nanoparticles in the entire matrix is displayed along the time step on the Figure 27. The nanoparticles mass could be computed by using equation (25), and the nanoparticles mass of all the matrix grids are summed up to obtain the total mass of nanoparticles. As the equation (25), the nanoparticles mass is related with nanoparticles concentration, grid porosity, water saturation, and grid volume.

At the early stage, the total mass of nanoparticles don't rise too much, because the water and nanoparticles just started to flow from the wellbore into the hydraulic fractures. When the time reach about 1.2×10^5 second, the growth rate significantly improves. After the time reaches about 1.0×10^8 second, the value of total nanoparticles approaches stable and keep almost the same, which proves no more nanoparticles could flow into the reservoir matrix. Two important points could be obtained from this curve. One is when does the nanoparticles flow reach stable, and the other one is how much the nanoparticles can flow into the reservoir matrix. In this reservoir model, about 4.72×10^{-5} kilogram enter the stimulated reservoir volume. Of course, the total value will be absolutely up to many different parameter, such as nanoparticles size and concentration, fractures pattern, and fracture conductivity.

$$M_t = \sum_i C_i \times \phi_i \times (S_w)_i \times VOL_i \quad (25)$$

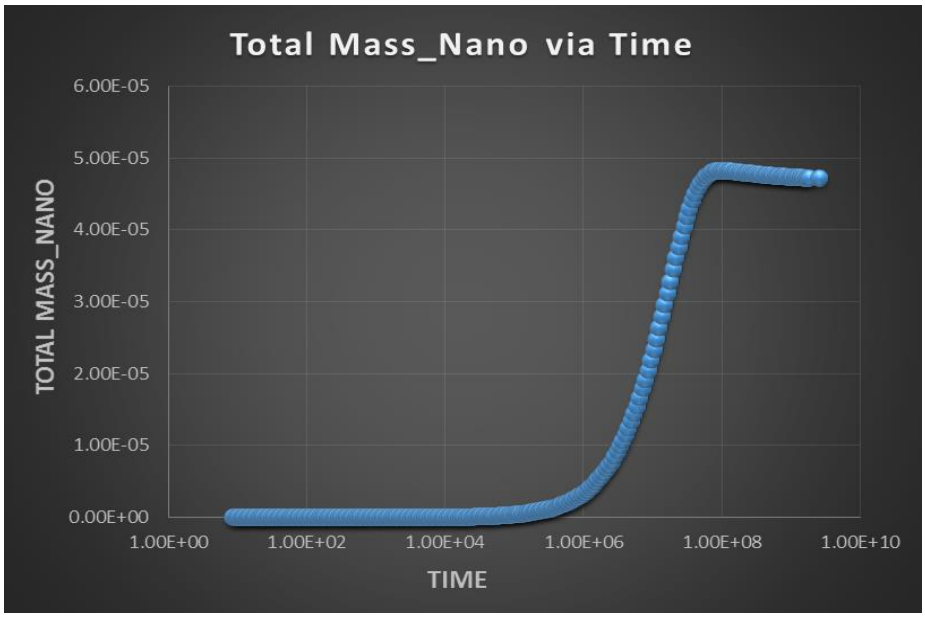

Figure 27: Total mass of nanoparticles at different time steps for reservoir model.

3.5 Results for Magnetism Analysis

Based on the magnetic theory and the equations above, the distribution of magnetic susceptibility in the shale reservoir could be computed. As the same reservoir matrix and the same mesh with the Figure 17, two numerical cases are performed and the results about the distribution of magnetic susceptibility are also shown in Figure 28 and 29 below: one is without magnetic nanoparticles in the wellbore and the other one consider the magnetic nanoparticles in the shale reservoir.

As we known, the magnetic nanoparticles are supposed to provide more source for the volume magnetic susceptibility. As proved in the figure 28 and 29, even though both graphs look almost the same, while they have different value range. The numerical case with magnetic nanoparticles clearly possesses higher value of magnetic susceptibility among the entire fractured reservoir than the model without magnetic nanoparticles, which supports and proves the potential of magnetic nanoparticle enhancing the NMR logging signal.

In the Figure 28 and 29 the value of magnetic susceptibility of natural fracture grids is less than that of inorganic grids, because the inorganic grids have much bigger volume than the natural fracture grids even though the natural fractures have higher water saturation. However, the volume magnetic susceptibility of natural and hydraulic fractures grids are much bigger, because their volume is far smaller than the volume of inorganic grids, as the equation (25). In other words, the final magnetization of fractures would be definitely large than the inorganic matter grids.

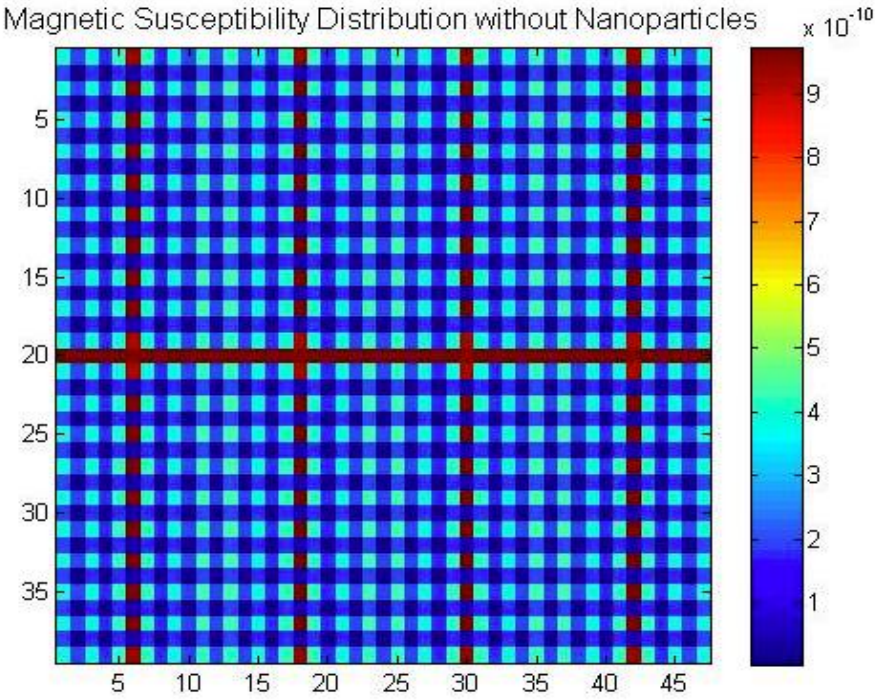

Figure 28: The distribution of magnetic susceptibility without magnetic nanoparticles for the reservoir model.

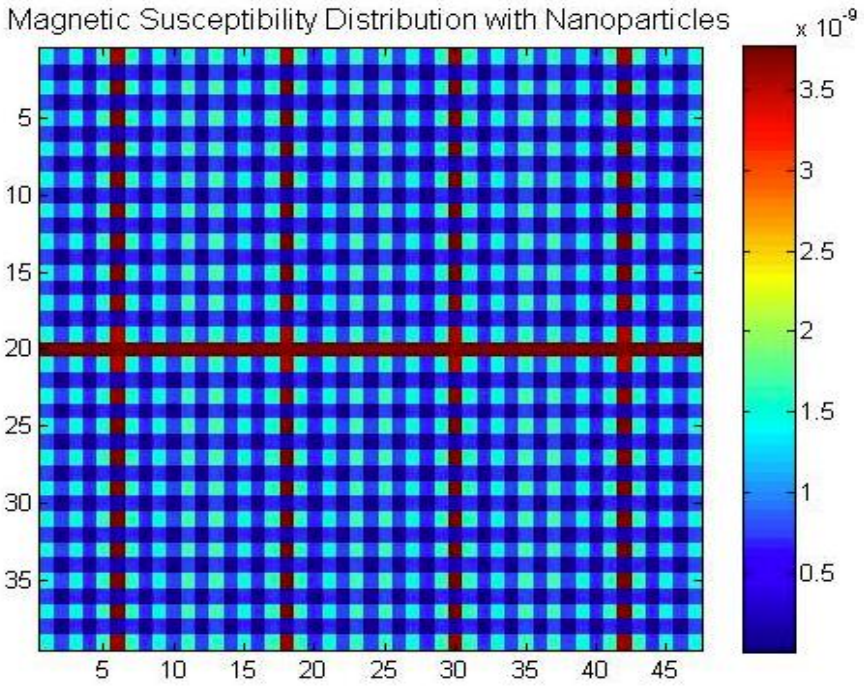

Figure 29: The distribution of magnetic susceptibility with magnetic nanoparticles for the reservoir model.

To specific explore the influence of magnetic nanoparticles on the distribution of magnetic susceptibility, the fifth layer of SRV as Figure 17 is chosen to show the change trend of total magnetic susceptibility in various medium. Two numerical cases with and without magnetic nanoparticles injected into stimulated reservoir volume are performed and compared to look into the results of magnetic susceptibility in the entire reservoir. The first case does not contain magnetic nanoparticles and the total volume magnetic susceptibility are comprised of water and methane. The second case includes the magnetic nanoparticles, so magnetic nanoparticles, water, and methane are the three contributor to the total volume magnetic susceptibility.

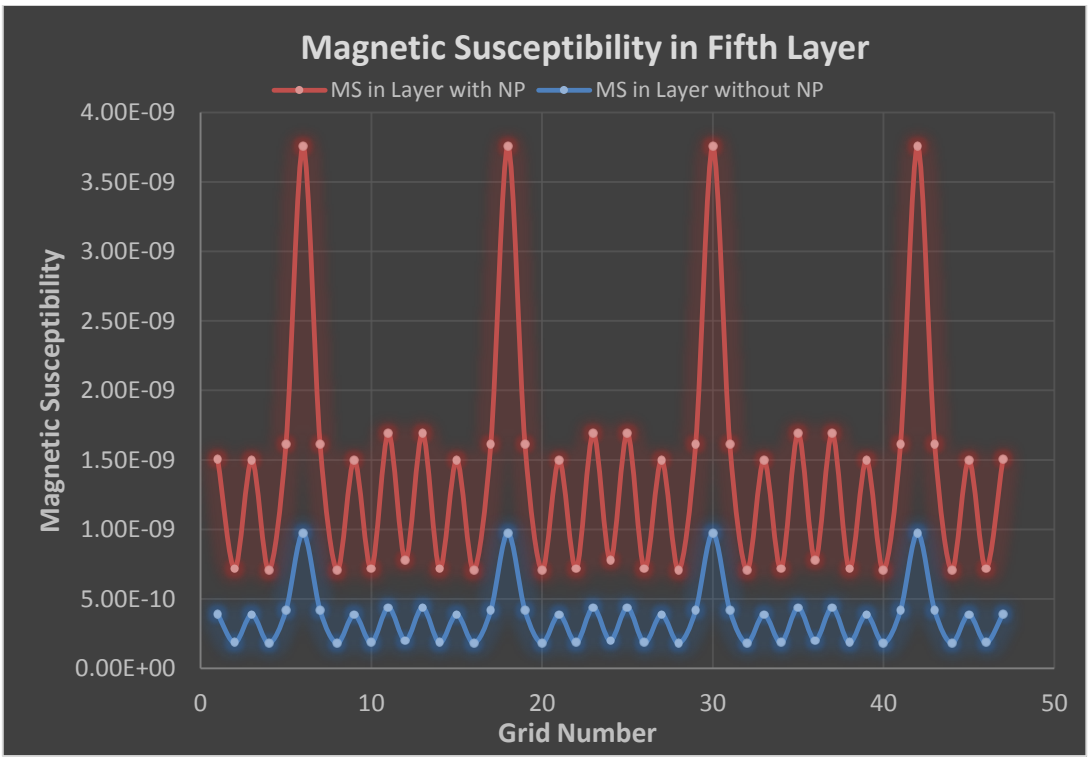

Figure 30: Magnetic susceptibility with and without Nanoparticles in fifth layer of reservoir model.

In the Figure 30 above, the magnetic susceptibility of the case with nanoparticles is obviously larger than the case without nanoparticles, which clearly proves nanoparticles can enhance the magnetic susceptibility of shale reservoirs. The red curve represents the case with nanoparticles and the blue curve stands for the case without nanoparticles. As the same in both two cases, the value of magnetic susceptibility is biggest for the hydraulic fracture grids and lowest in these natural fracture grids, because the hydraulic fracture grids contain bigger grid volume and more magnetic nanoparticles and water, while the volume of natural fracture girds are smallest.

Cheng et al. (2014) have conducted some experiments about measuring magnetic susceptibility to investigate the influences of magnetic nanoparticles. As in the Figure 31 below, several small liquid holders are built and placed, where simple water and the water with nanoparticles are alternately stored into the separate liquid holder. The value of magnetic susceptibility of each holder is measured and plotted in Figure 32, where two different run case are performed. In the both two run cases, the liquid holder containing magnetic nanoparticles obvious has higher NSL unit or magnetic susceptibility than that of holder without magnetic nanoparticles. In addition, the ratio of the case with magnetic nanoparticles to the case without nanoparticles is similar with the results of numerical reservoir model above. Based on the similar results, the experiment results confirm the results of numerical models and validate the accuracy and availability of the simulator we used.

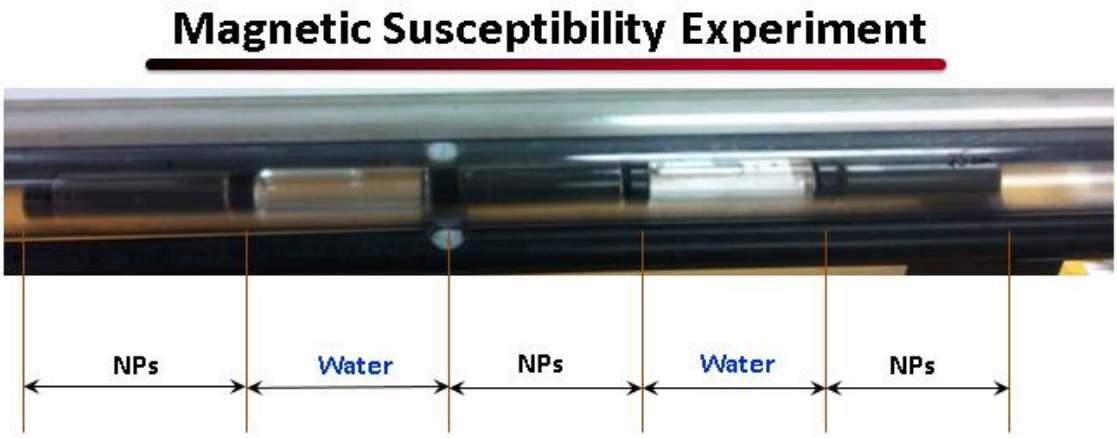

Figure 31: Magnetic susceptibility experiment (Cheng et al. 2014).

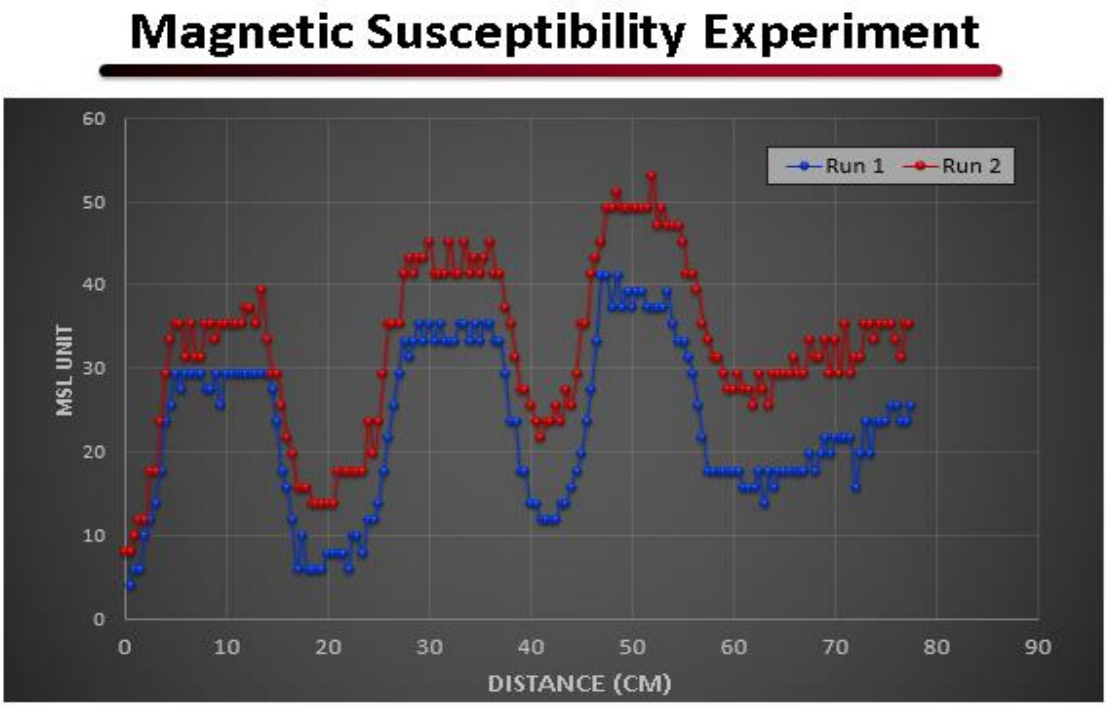

Figure 32: Magnetic susceptibility value along the distance (Cheng et al. 2014).

CHAPTER IV

CONCLUSIONS

This project has developed a mathematical model to investigate the nanoparticle transport in shale reservoirs; the modeling divides the reservoir into inorganic matter, organic matter, and fractures. It considers various flow mechanisms including Brownian diffusion, gas diffusion and desorption, Darcy flow, slippage flow, and capillary effects and their application to specific sub-media. This stimulator provides a solid description for modeling dynamic flow of gas, water and nanoparticles. 2D micro models was built to present the process of water and nanoparticles flowing into the matrix; then 2D macro models was created to display how far these particles could flow in the shale matrix. A reservoir model containing reservoir stimulating area was subsequently built to show the changing trend of water saturation and nanoparticle concentration at reservoir scale. Based on the diverse sources of magnetism, the distribution of volumetric magnetic susceptibility and magnetization of reservoir was computed and presented. Similar results were also obtained and compared on the same large reservoir models with and without magnetic nanoparticles. In addition, the results of the distribution of magnetic susceptibility were compared with the experimental data to validate the model's accuracy and predictability. Overall, Seven main conclusions are shown as following:

1. The mathematic model including sub-divided pores medium, various flow mechanisms, and mixed wettability was developed to describe the nanoparticles transport carried by a two-phase flow in shale reservoirs.

2. Nanoparticles could easily flow along fractures, whereas their transport into shale matrix is quite limited, only about 20 centimeters on our models, especially restricted for organic matter.

3. Brownian diffusion could contribute about 18% of the transport of nanoparticles, which means convection flow is the major flow contributor.

4. Refining the mesh offers the nearly same results for mass accumulation of nanoparticles which confirms the computation and accuracy of the models.

5. The magnitude of magnetic susceptibility is related to the permeability, water saturation and porous volume.

6. Magnetic nanoparticles can effectively increase the magnetic susceptibility and magnetization of shale reservoir.

7. The numerical results are compared with and also confirmed by the experimental results, which provides more confidence for applying magnetic nanoparticles to enhance signals to NMR logging devices.

REFERENCES

Alfi, M., Yan, B., Cao, Y. et al. 2014. Three-Phase Flow Simulation in Ultra-Low Permeability Organic Shale Via a Multiple Permeability Approach. Society of Petroleum Engineers. DOI: 10.15530/urtec-2014-1895733.

Ambrose, R.J., Hartman, R.C., Diaz Campos, M. et al. 2010. New Pore-Scale Considerations for Shale Gas in Place Calculations. Society of Petroleum Engineers. DOI: 10.2118/131772-MS.

Arogundade, O. and Sohrabi, M. 2012. A Review of Recent Developments and Challenges in Shale Gas Recovery. Society of Petroleum Engineers. DOI: 10.2118/160869-MS.

Arrighini, G.P., Maestro, M., and Moccia, R. 1968. Magnetic Properties of Polyatomic Molecules. I. Magnetic Susceptibility of H2o, Nh3, Ch4, H2o2. The Journal of Chemical Physics 49 (2): 882-889.

Bartko, K., Salim, A., Saldungaray, P. et al. 2013. Hydraulic Fracture Geometry Evaluation Using Proppant Detection: Experiences in Saudi Arabia. Society of Petroleum Engineers. DOI: 10.2118/168094-MS.

BBI Solution, Reference about molar concentration of nanoparticles. http://www.bbisolutions.com/support/technical-information/molar-concentration-of-nanoparticles/, Accessed in Aug. 2014.

Bird, R. B., Stewart, W. E., Lightfoot, E. N. 2007. Transport phenomena. John Wiley & Sons. ISBN 978-0-470-11539-8.

Bohr magneton, Wikipedia, Reference about Bohr magneton. http://en.wikipedia.org/wiki/Bohr_magneton, Accessed in Aug. 2014.

Boltzmann constant, Wikipedia, Reference about Boltzmann constant. http://en.wikipedia.org/wiki/Boltzmann_constant, Accessed in Aug. 2014.

Brooks, R.H. and Corey, A.T. 1964. Hydraulic Properties of Porous Media. Colorado State University, Hydrology Papers (5).

Cheng, K., Aderibigbe, A., Alfi, M., Heidari, Z., and Killough, J., 2014, Quantifying the impact petrophysical properties on spatial distribution of contrasting nanoparticle agents: Paper presented at the SPWLA 55th Annual Logging Symposium, Abu Dhabi, United Arab Emirates, May 18-22.

Cipolla, C.L., Lolon, E., Erdle, J.C. et al. 2009. Reservoir Modeling in Shale-Gas Reservoirs. Society of Petroleum Engineers. DOI: 10.2118/125530-MS.

Civan, F., 2010. Effective Correlation of Apparent Gas Permeability in Tight Porous Media, Transport in Porous Media, 82: 375-384.

Civan, F., Rai, C. S., Sondergeld, C. H. 2011. Shale-gas Permeability and Diffusivity Inferred by Improved Formulation of Relevant Retention and Transport Mechanisms, Transport in Porous Media, 86(3): 925-944.

Clarkson, C. R., Ertekin, T. 2010. A New Model for Shale Gas Matrix Flow Using the Dynamic-slippage Concept. AAPG Hedberg Conference, Austin, Texas, December 5-10.

Curtis, M.E., Ambrose, R.J., and Sondergeld, C.H. 2010. Structural Characterization of Gas Shales on the Micro- and Nano-Scales. Society of Petroleum Engineers. DOI: 10.2118/137693-MS.

Davis, A., The Chemistry of Health. US Department of Health and Human Services. Washington, D.C. 2009.

El-amin, M.F., Salama, A., and Sun, S. 2012. Modeling and Simulation of Nanoparticle

Transport in a Two-Phase Flow in Porous Media. Society of Petroleum Engineers. DOI: 10.2118/154972-MS.

El-Amin, M.F., Sun, S., and Salama, A. 2012. Modeling and Simulation of Nanoparticle Transport in Multiphase Flows in Porous Media: Co2 Sequestration.

Elimelech, M. and O'Melia, C.R. 1990. Kinetics of Deposition of Colloidal Particles in Porous Media. Environmental Science & Technology **24** (10): 1528-1536. DOI: 10.1021/es00080a012.

Energy Information Administration (EIA). Annual Energy Outlook Report 2013, http://www.eia.gov/forecasts/aeo/pdf/0383(2013).pdf, Accessed in Aug. 2014.

Esmaeili, A. Applications of Nanotechnology in Oil and Gas Industry. PETROTECH, New Delhi, India, January 11-15, 2009.

Feynman, R. P., There's Plenty Room at the Bottom: An Invitation to Enter a New Field of Physics. Annual Meeting of American Physical Society, Pasadena, CA, 1959.

Fisher, M.K., Heinze, J.R., Harris, C.D. et al., 2004, Optimizing Horizontal Completion Techniques in the Barnett Shale Using Microseismic Fracture Mapping. Society of Petroleum Engineers. DOI: 10.2118/90051-MS.

Fisher, M.K., Wright, C.A., Davidson, B.M. et al. 2002. Integrating Fracture Mapping Technologies to Optimize Stimulations in the Barnett Shale. Society of Petroleum Engineers. DOI: 10.2118/77441-MS.

Javadpour, F., Nanopores and Apparent Permeability of Gas Flow in Mudrocks (Shales and Siltstone). 2009. J. of Canadian Petroleum Tech., 48, pp 16-21.

Ju, B. and Fan, T. 2009. Experimental Study and Mathematical Model of Nanoparticle Transport in Porous Media. Powder Technology **192** (2): 195-202. DOI: http://dx.doi.org/10.1016/j.powtec.2008.12.017

King, G.E., Haile, L., Shuss, J.A. et al. 2008. Increasing Fracture Path Complexity and Controlling Downward Fracture Growth in the Barnett Shale. Society of Petroleum Engineers. DOI: 10.2118/119896-MS.

Kong, X. and M.M. Ohadi, 2010. Applications of micro and nano technologies in the oil and gas industry – overview of the recent progress. Proceedings of the Abu Dhabi International Petroleum Exhibition Conference, Nov. 1-4, Abu Dhabi, UAE, pp: 1-4. DOI: 10.2118/138241-MS.

Kundert, D.P. and Mullen, M.J. 2009. Proper Evaluation of Shale Gas Reservoirs Leads to a More Effective Hydraulic-Fracture Stimulation. Society of Petroleum Engineers. DOI: 10.2118/123586-MS.

Lu, A.H., Salabas, E.L., Schüth, F. 2007. Magnetic Nanoparticles: Synthesis, Protection, Functionalization, and Application. Angew. Chem. Int. Ed. 46, 1222–1244

Magnetic Susceptibility, Wikipedia, Reference about magnetic susceptibility. http://en.wikipedia.org/wiki/Magnetic_susceptibility, Accessed in Aug. 2014.

Matteo, C., P. Candido, R. Vera and V. Francesca, 2012. Current and Future Nanotech Applications in the Oil Industry. Am. J. Applied Sci., 9: 784-793.

Mayerhofer, M.J., Lolon, E., Warpinski, N.R. et al. 2010. What Is Stimulated Rock Volume? Society of Petroleum Engineers. DOI: 10.2118/119890-MS.

Methane, Wikipedia, Reference about chemical data on methane. http://en.wikipedia.org/wiki/Methane_(data_page), Accessed in Aug. 2014.

Millington, R. J. and J. M. Quirk, 1961. Permeability of porous solids. Trans. Faraday Soc. 57:1200-1207.

Moridis, G.J., M.B. Kowalsky, and K. Pruess, TOUGH+HYDRATE v1.0 User's Manual: A Code for the Simulation of System Behavior in Hydrate-Bearing

Geologic Media, Report LBNL-149E, Lawrence Berkeley National Laboratory, Berkeley, Calif., 2008.

Paramagnetism, Wikipedia, Reference about Paramagnetism. http://en.wikipedia.org/wiki/Paramagnetism, Accessed in Aug. 2014.

Sbai, M.A. and Azaroual, M. 2011. Numerical Modeling of Formation Damage by Two-Phase Particulate Transport Processes During Co2 Injection in Deep Heterogeneous Porous Media. Advances in Water Resources **34** (1): 62-82. DOI: http://dx.doi.org/10.1016/j.advwatres.2010.09.009

Shabro, V., Torres-Verdin, C., and Sepehrnoori, K. 2012. Forecasting Gas Production in Organic Shale with the Combined Numerical Simulation of Gas Diffusion in Kerogen, Langmuir Desorption from Kerogen Surfaces, and Advection in Nanopores. Society of Petroleum Engineers. DOI: 10.2118/159250-MS.

SPE PetroWiki, Nuclear Magnetic Resonance (NMR) Logging. http://petrowiki.org/Nuclear_magnetic_resonance_(NMR)_logging, Accessed in Aug. 2014.

Swami, V. 2012. Shale Gas Reservoir Modeling: From Nanopores to Laboratory. SPE Annual Technical Conference and Exhibition. San Antonio, Texas, USA.

Swami, V. and Settari, A. 2012. A Pore Scale Gas Flow Model for Shale Gas Reservoir. Society of Petroleum Engineers. DOI: 10.2118/155756-MS.

The Engineering ToolBox, Reference about density for common gases. http://www.engineeringtoolbox.com/gas-density-d_158.html, Accessed in Aug. 2014.

Wang, F.P. and Reed, R.M. 2009. Pore Networks and Fluid Flow in Gas Shales. Society of Petroleum Engineers. DOI: 10.2118/124253-MS.

Warpinski, N.R., Mayerhofer, M.J., Vincent, M.C. et al. 2008. Stimulating Unconventional Reservoirs: Maximizing Network Growth While Optimizing Fracture Conductivity. Society of Petroleum Engineers. DOI: 10.2118/114173-MS.

Wu, Y. S. and Pruess, K., 2000, Numerical Simulation of Non-isothermal Multiphase Tracer Transport in Heterogeneous Fractured Porous Media: Advances in Water Resources, 23, pp. 699-723.

Yan, B., Alfi, M., Wang, Y. et al. 2013c. A New Approach for the Simulation of Fluid Flow in Unconventional Reservoirs through Multiple Permeability Modeling. Society of Petroleum Engineers. DOI: 10.2118/166173-MS.

Yan, B., Killough, J.E., Wang, Y. et al. 2013b. Novel Approaches for the Simulation of Unconventional Reservoirs. Society of Petroleum Engineers. DOI: 10.1190/URTEC2013-131.

Yan, B., Wang, Y., and Killough, J.E. 2013a. Beyond Dual-Porosity Modeling for the Simulation of Complex Flow Mechanisms in Shale Reservoirs. Society of Petroleum Engineers. DOI: 10.2118/163651-MS.

Yu, H., 2012, Transport and Retention of Surface-modified Nanoparticles in Sedimentary Rocks: Ph.D. Dissertation, The University of Texas at Austin, USA.

Yu, J., Berlin, J.M., Lu, W. et al. 2010. Transport Study of Nanoparticles for Oilfield Application. SEP International Conference on Oilfield Scale, Aberdeen, UK.

Yu, W. and Sepehrnoori, K. 2013. Optimization of Multiple Hydraulically Fractured Horizontal Wells in Unconventional Gas Reservoirs. Society of Petroleum Engineers. DOI: 10.2118/164509-MS.

Zhang, T., 2012, Modeling of Nanoparticles Transport in Porous Media: Ph.D. Dissertation, The University of Texas at Austin, USA.

Zhang, T., Ellis, G.S., Ruppel, S.C. et al. 2012. Effect of Organic-Matter Type and Thermal Maturity on Methane Adsorption in Shale-Gas Systems. Organic Geochemistry 47(0): 120-131. DOI: http://dx.doi.org/10.1016/j.orggeochem.2012.03.012.